Radar Observations of Asteroids 7 Iris, 9 Metis, 12 Victoria, 216 Kleopatra, and 654 Zelinda

DAVID L. MITCHELL, STEVEN J. OSTRO, AND KEITH D. ROSEMA
Jet Propulsion Laboratory, California Institute of Technology, Pasadena, California 91109
e-mail. mitchell@think.jpl.nasa.gov

R. SCOTT HUDSON
Department of Electrical Engineering, Washington State University, Pullman, WA 99164

DONALD B. CAMPBELL
National Astronomy and Ionosphere Center, Cornell University, Ithaca, NY 14853

AND

JOHN F. CHANDLER AND IRWIN I. SHAPIRO
Harvard-Smithsonian Center for Astrophysics, Cambridge, MA 02138

27 February 1995

submitted to *Icarus*

35 pages

21 figures

6 tables

key words: asteroids, radar, surfaces, composition

ABSTRACT

We report 13-cm wavelength radar observations of the main-belt asteroids 7 Iris, 9 Metis 12 Victoria, 216 Kleopatra, and 654 Zelinda obtained at Arecibo between 1980 and 1989. The echoes are highly polarized yet broadly distributed in Doppler frequency. indicating that our targets are smooth on decimeter scales but very rough on some scale(s) larger than about one meter. The echo spectra are generally consistent with existing size, shape, and spin information based on radiometric, lightcurve, and occultation data, except that Victoria spectra from two apparitions conflict with the only published pole direction for that target. All of our targets possess distinctive radar signatures that reveal large-scale topography. Reflectivity spikes within narrow ranges of rotation phase suggest large flat regions on Iris, Metis, and Zelinda, while bimodal spectra imply nonconvex, possibly bifurcated shapes for Kleopatra and Victoria, Kleopatra has the highest radar albedo yet measured for a main-belt asteroid, indicating a high metal concentration and making Kleopatra the best main-belt candidate for a core remnant of a differentiated and subsequently disrupted parent body. Upon completion of the Arecibo telescope upgrade. there will be several opportunities per year to resolve main-belt asteroids with hundreds of delay-Doppler cells, which can be inverted to provide estimates of both three dimensional shape and radar scattering properties.

1. INTRODUCTION

The shapes, spins, and surface properties of main-belt asteroids (MBAs) are key boundary conditions on theories for the collisional histories of individual objects and the entire asteroid popu lation. A variety of methods are employed at optical and infrared wavelengths to deduce the shapes and spins of MBAs, despite their small angular sizes (~ 0.1 arcsec). Photometric lightcurves are reliable sources of simple shape constraints and rotational information for hundreds of asteroids (Magnusson et *al.* 1989 and references therein). Speckle interferometry (Drummond and Hege 1989 and references therein, Tsvetkova *et al.* 1991, McCarthy *et al.* 1994) and adaptive optics (Saint-Pé *et al.* 1993a, b) can yield images with $\lesssim 0.1$ arcsec resolution, sufficient to reveal the overall shapes of some of the largest MBA's. Occultation observations can furnish direct dimensional constraints and, if chords are densely sampled, detailed limb profiles (Minis and Dunham 1989. and references therein). Of course. the most powerful technique by far is spacecraft reconnaissance, as demonstrated by Galileo images that revealed the irregular, heavily cratered surfaces of Gaspra and Ida; however, it is unlikely that such missions will provide images of a large number of asteroids in the near term.

Radar observations can obtain useful spatial resolution of main-belt asteroids if the echoes are strong enough. The spatial resolution arises from the ability to resolve the echo in time delay and Doppler frequency, and does not depend on the angular size of the target. In practice, such observations have been limited by the sensitivity of available telescopes, and almost all MBA radar measurements are resolved only in Doppler frequency, providing one-dimensional images that can be thought of as scans of radar brightness taken through a slit parallel to the target's projected spin vector. For the bulk of extant observations. the signal-to-noise ratio (SNR) of an optimally filtered sum of all spectra obtained in an experiment is less than 10. providing marginal spatial resolution. For experiments with much higher SNR. the spectra provide unique information about size, shape. and spin vector, but even the lowest SNR observations are useful because disc-integrated radar properties constrain macroscopic roughness and near-surface bulk density.

Ostro, Campbell, and Shapiro (1985, henceforth OCS85) reported initial results from Arecibo (13-cm, 2380-MHz) radar observations of 20 MBAs. Their principal results included (i) polarization ratios that indicate, for almost all their targets, a deficit of near-surface roughness within an order of magnitude of the wavelength, (ii) broad echo spectral shapes that require considerable roughness at some scale(s) large compared to the wavelength, and (iii) a five-fold variation in radar albedo, implying metal concentrations ranging from nearly zero to nearly unity if the surfaces all have regoliths with porosities like those on the Moon. Since that paper was published, the list of radar-detected MBAs has increased by 50% and several objects have been observed during more than one apparition.

Here we present detailed analyses of all radar observations of 7 Iris, 9 Metis, 12 Victoria, 216 Kleopatra and 654 Zelinda conducted at Arecibo during 1980-1989. Echoes from each of these asteroids show evidence for large-scale topography. For Iris, Metis, and Zelinda, Doppler-resolved spectral features appear over small intervals of

rotation phase, probably due to reflections from large flat regions. For Kleopatra and Victoria, bimodal spectra in restricted phase internals indicate nonconvex, possibly bifurcated shapes. Our observations yield new constraints on pole direction and surface properties for all five objects.

In the next section we describe our observations and data reduction, and give an overview of our strategies for data analysis and physical inference. In Section 3, we present radar results for each asteroid in turn, gearing our analysis to the particular combination of available echo strength, rotation phase coverage, and non-radar prior information about physical properties. In Section 4 we discuss the ensemble of results and their implications for asteroid science. We conclude by describing immediate prospects for observations of these objects with the upgraded Arecibo radar,

2. OBSERVATIONS ANI) DATA REDUCTION

Observational and data reduction techniques were very similar to those described by Ostro *et al.* (1983 and 1992). Briefly, each transmit-receive cycle. or run, yielded echo power spectra that we blocked into 4-minute sums. Each run's receive interval typically lasted several seconds less than the round-trip echo time delay (RTT), between 14 and 24 minutes for our observations. Table I lists first and last observation dates, total numbers of runs, and average values of right ascension, declination, and distance for each apparition. The. post-1981 observations used a two-channel receiving system for simultaneous recording of echoes in the same sense of circular polarization as transmitted (the SC sense) and in the opposite (OC) sense. (The 1980 Iris observations used a single-channel system, which was switched between 0(and SC in alternate runs.) The helicity of circular polarization is reversed upon reflection from a surface that is smooth on all scales within about an order of magnitude of the wavelength, but SC echo power can arise from single backscattering from a rough surface. from multiple scattering, or from subsurface refraction. The circular polarization ratio μ_C = SC/OC is thus a measure of the near-surface structural complexity, or "roughness," at scales near the wavelength.

Echo power is given by $P_R = P_T G_T G_R \lambda^2 \sigma/(4\pi)^3 R^4$, where P_T *is the* transmitted power, G_T and G_R are the antenna gains during transmission and reception, λ is the observing wavelength, R is the radar-target distance, and σ is the radar cross section (either OC or SC), defined as 4π times the backscattered power per steradian per unit incident flux at the target. Echo power was measured as a function of frequency relative to the Doppler frequency of hypothetical echoes from the center of mass (COM) as predicted by site ephemerides. The uncertainties in the Doppler-prediction ephemerides were small compared with the data's frequency resolution.

We normalized each of our 4-minute spectra to the. standard deviation of the receiver noise to facilitate the formation of weighted sums of spectra taken with different values of antenna gain, transmitter power, system temperature, target distance, and integration time. Uncertainties in estimates of radar cross section are due primarily to systematic errors in calibration of antenna gain (as a function of elevation and azimuth), transmitter power, and

system temperature, as well as pointing accuracy, which varies over a variety of time scales. Our experience during the 1980s with observations of a variety of radar targets leads us to believe that for the most part, the absolute uncertainty in radar cross section estimates is between 20% and 50'%, while relative uncertainties are half as large. Most systematic effects cancel for μ_C, and statistical uncertainty from the propagation of receiver noise (Appendix I of Ostro *et al.* 1983) dominates our quoted errors. The time-bandwidth products for all spectra presented in this paper are >>100, and the noise obeys Gaussian statistics. Our method for estimation and removal of the mean background of the receiver noise was described most recently by Ostro *et al. (1992).* Typically, several runs were obtained each day over a span of several days to provide spectra at different rotation phases and to increase the total SNR. For each radar apparition, the target's plane-of-sky motion was very small (Table I). The useful rotation phase resolution is restricted by the available sampling in rotation phase and the echo SNRS and is different for each target,

3. DATA ANALYSIS

An echo's strength and polarization, and its distribution in Doppler frequency and time delay contain information about the target's characteristics on size scales from its overall dimensions down to the microscopic. It is useful to imagine a hierarchy of scales:

$$\text{wavelength} \ll \text{facet} \ll \text{tile} \ll \text{asteroid}$$

where "tile" implies the effective spatial resolution of the data and/or an assumed model. Most radar-detected asteroids, including those discussed in this paper, have low circular polarization ratios ($\mu_C \sim$ O. 1), which indicates that most of the OC echo power is due to single back-reflections from surface elements, or "facets," that are smooth on all scales within about an order of magnitude of the wavelength (OCS85).

For targets with low μ_C, the OC radar albedo ($\hat{\sigma}_{OC} = \sigma_{OC}/A_P$, *with* A_P *the* target's projected area) can be related to the Fresnel power reflection coefficient at normal incidence (R) via:

$$\hat{\sigma}_{OC} \equiv \frac{\sigma_{OC}}{A_P} = gR \quad , \tag{1}$$

where the gain factor g depends on the target's orientation, its gross shape, the distribution of surface slopes with respect to that shape, and on the degree of wavelength-scale, near-surface roughness. For a sphere with μ_C = O, the gain factor is unity, and one can think of g's departure from unity as quantifying how the distribution of facet tilts with incidence angle differs from that of a sphere. For most large main-belt asteroids, g is expected to be within a few tens of percent of unity (OCS85), so that $\hat{\sigma}_{OC}$ provides a reasonable first approximation to R. For dry, particulate mixtures of rock and metal with particle sizes $< \lambda/100$, R depends strongly on bulk density, which in turn is a function of the porosity, the metal weight fraction, and the specific gravities of the rock and metal phases.

An echo's instantaneous edge- to-edge bandwidth B at rotation phase ϕ can be written:

$$B(\phi, \delta) = \frac{4\pi D(\phi)}{\lambda P} \cos(\delta) \qquad (2)$$

where D is the breadth normal to the radar line of sight of the asteroid's pole-on silhouette, δ is the target-centered declination of the radar and P is the apparent rotation period, Each target's rotation period is known quite well (Lagerkvist et *al.* 1989 and references therein) and the contribution of plane-of-sky motion to the apparent rotation was negligible for all our observations; therefore, we treat our bandwidth estimates as joint constraints on $D(\phi)$ and δ. Our ability to discern the spectral edges of an echo and hence the perceptibility of rotational bandwidth variations depends on the shape and radar scattering properties of the target and on the SNR, which for the targets discussed here is not very high. In any event, the observed bandwidth can never be greater than the maximum bandwidth. $B_{max}(\delta) = [4\pi D_{max}/\lambda P] \cos\delta$, corresponding to the maximum breadth of the target's pole-on silhouette.

One goal of asteroid astronomy is the development of realistic, detailed shape models. For several of our targets, ellipsoid models based on photometric lightcurves, occultations, and infrared radiometry provide approximations that refine radar albedo estimates and also provide a *priori* estimates of $B_{max}(\delta)$. When there is sufficient confidence in knowledge of an echo's bandwidth. the spectral shape constrains surface structural characteristics at both facet and tile scales. For example, one measure of surface roughness on scales $\gtrsim 10\lambda$ is the fractional half-power bandwidth B_{HP}/B_{max}. Radar echoes from the Moon, with $B_{HP}/B_{max} \sim 0.1$, are dominated by specular reflections from surface elements near the sub-radar point. OCS85 found that B_{HP}/B_{max} *-0.5* for the very -low-μ_C targets Ceres and Pallas, indicating surfaces that are much rougher than the lunar surface at some scale(s) greater than a few meters.

With adequate SNR, echo bandwidth and spectral structure as functions of rotation phase can constrain an asteroid's shape by revealing topographic features. Higher SNR cases may warrant using the echoes *to* estimate the shape. The number of shape parameters constrained by the data is dictated by the SNR, the Doppler resolution, and the orientation coverage of the data. Some approaches used to model Earth-crossing asteroid echoes (e.g., Ostro et *a/. 1990,* Hudson and Ostro 1994) have limited applicability y to the observations reported here. All such approaches parameterize the surface's average angular scattering law [$\sigma_o(\theta) = d\sigma/dA$, where dA is an element of surface area and θ is the angle of incidence], which quantifies effects of structure at facet scales. Simpson and Tyler (1982) described efforts to infer facet slope statistics from measurements of $\sigma_o(\theta)$ within the framework of various definitions of slope probability density functions. For example, in modeling echoes from Pallas, OCS85 assumed a spherical shape and a scattering law proportional to $\exp(-s_0^{-2}\tan^2\theta)/\cos^4\theta$, where SO is the adirectional rms slope. Parker's (1973) one-dimensional probability y density function is implicit, and Gaussian height-distribution and surface autocorrelation functions are assumed. All other modeling of asteroid echoes to date has used an empirical $\cos^n\theta$ law, for which $n = 1$ corresponds to geometric scattering (radar brightness proportional to projected area), n = 2 to Lambert limb darkening, and higher values to more specular backscattering. Estimates of the radar scattering

law exponent for two Earth-crossing asteroids yield $n \approx 2$ for 1685 Toro (Ostro *et* al. 1983) and n = 2.8* 0.3 for 4769 Castalia (Hudson and Ostro 1994). If a Parker probability density function is assumed, then a $\cos^n\theta$ scattering law implies $s_0 = \sqrt{2/n}$, or $\tan^{-1}(s_0)$ =45° and 40° for those two objects (see the Appendix).

4. RESULTS

In this section. we begin the discussion of each target by assessing the available non-radar information about size, shape, and spin vector from radiometric, lightcurve, and occultation observations. These constraints are summarized in Table II for ease of reference. For Iris, Metis, and K leopatra, analyses of multi-apparition lightcurves have produced estimates of pole direction as well as simple shape constraints in the form of model ellipsoid axis ratios (a/b and *b/c,* where $a \geq b \geq c$ and rotation is about the shortest axis). Size constraints derived from a combination of optical and infrared data are available for Iris, Victoria, Zelinda and Kleopatra (Tedesco and Veeder 1992). Occultation observations contribute prior information about the sizes and shapes of Metis and Kleopatra.

Galileo's encounters with Gaspra and Ida have provided two tests for evaluating groundbased predictions for size, shape, and spin vector. Although both asteroids are irregularly shaped, ellipsoid models derived from groundbased VIS/IR observations furnished accurate predictions of size, elongation and (ambiguities aside) pole direction (Magnusson *et al.* 1992, Binzel *et al.* 1993, Belton *et al.* 1994). We have studied the published nonradar constraints on our targets' geometric properties and in several cases have settled on an *a priori* ellipsoid model as the starting point of our analysis.

Iris

Magnusson's (1986) analysis of Iris lightcurves yielded a model ellipsoid with *a/b*= 1.18, *b/c*= 1.41, and a pole direction with ecliptic longitude and latitude (λ, β) of either (15° ± 5“, +25”* 15”) or (195° ± 5°. +15° ± 150). The lightcurve coverage for Iris is such that uncertainties in the axis ratios are believed to be c 0.1 (Magnusson 1990). Another lightcurve analysis (Zappalà and Di Martino 1986) yielded a model ellipsoid with *a/b = 1.19, b/c* = 1.21, and possible pole directions of (18° ± 5°, +33° ± 7°) and (193” ± 4“, +16° ± 8“). These analyses are in agreement, except for their estimates of *b/c,* possibly because of different assumptions about the optical scattering properties of Iris' surface. Magnusson assumed geometric scattering, while Zappalà and Di Martino applied an empirical correction factor based on the laboratory work of Barucci *et al. (1984).* Magnusson (1990) argues convincingly that geometric scattering is a better approximation to the “true” scattering law than is the model of Barucci et *al.. so we* will adopt Magnusson's model.

Goldstone-VLA radar aperture synthesis observations of Iris (de Pater *et al.* 1994) removed the ambiguity in the pole direction in favor of the solution (λ = 15”, β = +25°). This pole direction corresponds to a subradar latitude $\delta \approx$ 19° ± 8° during the IRAS observations, which provided a radiometric diameter of 200 ± 10 km (Tedesco and

Veeder 1992). The average projected area of Magnusson's ellipsoid model during those observations would be the same as that of a 200-km sphere if the ellipsoid's dimensions were 260x220x155 km. We adopt this as a working model for Iris, with a 15% uncertainty in each dimension, which is intended to include the quoted uncertainties in the radiometric diameter and the model ellipsoid's axis ratios, possible systematic bias in scaling the ellipsoid using the radiometric diameter (Brown 1985), and uncertainty in the asteroid's orientation at the time of the IRAS observations.

Figure 1 shows weighted sums of echo spectra obtained in 1980 and 1984 smoothed to a resolution of 30 Hz, Fig. 2 reproduces a weighted-sum spectrum from recently reported 1991 Goldstone 3.5-cm observations (de Pater *et al.* 1994) smoothed to 240 Hz, and Figs. 3 and 4 show sums of spectra with selected rotation phase groups for 1980 and 1984. As depicted in polar plots inset into the. figures, each spectrum represents a weighted average of spectra from short integration times (4-minute blocks or individual runs -- see captions). In the polar plots, the standard deviation of the noise for each spectrum that contributes to the sum is represented by a radial "error bar" at the corresponding relative rotation phase. The rotation phase origins are arbitrary and do not correspond to any particular orientation of the model ellipsoid. The SNR's of the spectra in Figs. 3 and 4 preclude detection of rotational bandwidth variations as small as those predicted by the model ellipsoid.

The horizontal extents of the shaded boxes in Figs. 1 and 2 encompass interval estimates for spectral edge locations based on $B_{max}(\delta)$ for the nominal ellipsoid model and pole direction (Table II) and the uncertainties therein. The apparent extents of the OC spectra (i.e., the bandwidths between first zero crossings) are consistent with the prior constraints. These spectra, therefore, are best described as very broad ($B_{HP}/B \geq 0.5$), and we can conclude with reasonable confidence that Ins is rough at some scale(s) no smaller than the wavelength. However, Iris' low circular polarization ratio (Table III) indicates that most of the echo power arises from single back-reflections from facets whose sizes and radii of curvature are large compared to λ. Thus the detection of echo power near the spectral edges, far from the center of the asteroid's disc, seems to require considerable roughness at some scale(s) greater than a few meters.

Our 1984 Iris spectra show evidence for roughness at topographic scales, that is, scales that are not negligible compared with the asteroid's overall dimensions. A narrow spike centered near -300 Hz can be seen in the "group 1" spectrum of Fig, 4. The available SNR does not allow precise estimation of the attributes of this spike, but we have determined the optimal filtering in rotation phase and Doppler frequency that maximizes the spike's SNR. An average of six consecutive spectra covering a phase interval of $\Delta\phi \approx 13°$. smoothed to 90 Hz resolution. yields SNR ≈ 8 for the spike. Because of limited SNR and a data gap immediately following this interval, we consider this estimate to be only a crude one for the feature's extent in rotation phase. Figure 5 shows this spectrum and similarly processed spectra before and after the appearance of the radar spike. The 90-Hz frequency filter corresponds to a distance, measured normal to the plane containing Iris' spin vector and the radar line of sight, of-25 km, which sets a lower bound on one dimension of the region responsible for the spike. If this feature were due to a region of

unusually high intrinsic radar reflectivity, we would expect to see it migrate from left to right as rotation brought it from positive to negative Doppler frequencies. The feature's presence in a restricted phase interval indicates that the surge in brightness is due to geometry, *i.e.,* a temporary surge in surface area *oriented* normal *to* the radar. That *is.* there must be a large region on Iris with surface facets more or less parallel to each other. Various detailed configurations of facets are obviously possible, but the most plausible physical picture is of a continuous, fairly hat region.

Table III shows estimates of Iris' OC radar cross section, OC radar albedo, and circular polarization ratio from the 1980, 1984, and 1991 experiments. The radar cross section (σ_{OC}) is calculated from a weighted average of available spectra, and the radar albedo (kc) is estimated by dividing σ_{OC} by the projected area of the nominal *a priori* ellipsoid averaged over all rotation phases. The quoted uncertainties (in parentheses) include all known sources of error, including the fact that the phase for the. ellipsoid's minimum-bandwidth orientation is not known. The weighted average of all radar albedo estimates for Iris is $\hat{\sigma}_{OC} = 0.11 \pm 0.03$. This and values for our other four targets will be discussed in Section 4. The 13-cm estimate of μ_C from 1980 is less than either the 3.5-cm estimate at a comparable subradar latitude or the 1984 estimate obtained with a more equatorial view. Discrepancies in estimates of μ_C for other multi-year asteroid radar data sets are rare, even at the low level of significance here, so we take these numbers to suggest the possibility or either regional or scale-dependent variations in small-scale structure.

Metis

Since the mid 1980's, three separate lightcurve analyses (all assuming geometric optical scattering) have provided triaxial ellipsoid models and pole directions for Metis. Zappalà and Knežević (1984) found axis ratios of $a/b = 1.32$ and $b/c = 1.34$ and possible pole directions with ecliptic coordinates of Z1 = (2"* 6°. +26" ± 6°) and Z2 = (186° ± 8°, +43° ± 60). Magnusson (1990) found axis ratios of $a/b = 1.27$ and b/c= 1.26 and a pole direction of either Ml = (0° ± 5°, +20° ± 10") or M2 = (180° ± 5", +30" ± 10'). As for Iris, uncertainties in Magnusson's axis ratios are believed to be < 0.1. Finally, Drummond *et al.* (1991) obtained axis ratios of $a/b = 1.27 \pm 0.02$ and $b/c = 1.24 * 0.02$ and a pole direction within 8" of either D1 = (0°, +7°) or D2 = (181°, +230). The model axis ratios are within Magnusson's quoted uncertainties, so we will adopt Magnusson's axis ratios with conservative uncertainties of 0.1. The pole longitudes agree to well within the quoted uncertainties, but there is a significant dispersion in the pole latitudes, which may be due in part to solution refinements as additional lightcurve data became available.

Metis was not observed by IRAS, but occultation chords from 1984 are fit by an ellipse with overall dimensions of 21 OX17O km (Kristensen 1984; see also Minis and Dunham 1989). The sky projections of the poles listed above are aligned within 40" of the occultation ellipse's long axis, suggesting some foreshortening of the asteroid's longest dimension. Given the above pole directions and their uncertainties, the view during the occultation was sufficiently

close to pole-on (49° < |δ| c 83") that the projection of Magnusson 's ellipsoid would be at least 93% as long as the ellipsoid itself. In light of this information, we adopt as an *a priori* shape model an ellipsoid with dimensions within 15% of 215X170X135 km.

Figure 6 shows weighted sums of echo spectra obtained in 1984 and 1986. Predicted ranges for B_{max} based on the adopted a *priori* shape model and the pole directions listed above are shown by shaded boxes for comparison with the apparent spectral edges (the innermost zero crossings) for each year. The various pole solutions give identical predictions for δ and hence B_{max} for the 1986 apparition, but different predictions for 1984. Whereas the 1984 spectrum's edges seem to favor the D 1, D2, and M2 pole solutions, an unusual shape and/or a highly specular radar scattering law could conceivably produce a spectral shape with weak wings that would be obscured by the noise, In any event. the currently available radar data cannot resolve the pole ambiguity for Metis.

Figs. *7* and *8 show* sums of spectra within selected rotation-phase groups for each year. As with Iris, a radar spike in Metis spectra from the 1984 apparition is seen within a limited rotation phase interval. This spike dominates the "group 5" spectrum in Fig. 7 and is sufficiently strong that it can be detected in two adjacent rotation phase sub-groups (Fig. 9 [a] and [b]) spanning -24° of rotation phase. However, the SNR is insufficient to detect the spike at rotation phases immediately adjacent to that range (e.g., Fig. 9 [c]). so we cannot discern rotation phase boundaries for the feature. The spike's height is maximized by filtering to a resolution of 50 Hz, which corresponds to a linear dimension of at least 9.2 km / cos δ. The M2 pole direction predicts δ = -69° ± 110. which corresponds to 26 (+27,-9) km. or 12 (+27, -9) % of the *a priori* ellipsoid's longest dimension (vs. -25 km and ~10% for the Iris feature). The D1 and D2 pole directions predict |δ| = 75" ± 11°, which corresponds to 36 (+95, -15) km, or 17 (+44, -7) % of the *a* priori ellipsoid's longest dimension. Our estimates of μ_C for Metis (Table HI) are similar to those for Iris, so our inferences about surface structure on Iris seem broadly applicable to Metis. However, the Metis glint was seen during a more pole-on apparition ($|\delta|_{Metis} \gtrsim 50$") and the Iris glint was seen during a more equatorial apparition ($\delta_{Iris} = 19° \pm 8$"). Therefore, the putative flat regions responsible for the glints must have very different orientations with respect to the two asteroids' equatorial planes.

Zelinda

IRAS observations of Zelinda yielded a radiometric diameter of 127 ± 4 km, and lightcurves have established a rotation period of 31.9 hours, hut no a *priori* shape models or pole-direction constraints have been published for this object. Nonetheless, Zelinda's lightcurves exhibit peak-to-valley brightness variations of ~0.3 magnitudes (Schober 1975). Noting that Iris' lightcurves have similar amplitudes and that projected area variations of iris' *a priori* ellipsoid model are as large as 18%, we adopt a 20% uncertain y for Zelinda's projected area.

We observed Zelinda on Jan 17 and 18, 1988, completing four runs on the first date and five on the second, Each run yielded four OC/SC pairs, one from each of four, four-minute accumulations. Figure 10 plots OC weighted-sum spectra for (a) the nine runs, (b) the two dates, and (c) the entire experiment. The two dates spanned two sections of rotation phase about 82° apart: 166°-191° on Jan. 17 and 93°-100" on Jan. 18. Our phase origin is arbitrary — we do not know the correspondence between our phases and those of lightcurve extrema.

For a target with Zelinda's rotation period, Eq. 2 can be rewritten to relate instantaneous bandwidth (B, Hz) to breadth *(D, km):* $B = 0.869\ D \cos\delta$, *so* estimation of B places a joint constraint on D and b. The innermost zero crossings of the spectrum in Fig. 10 (c) give B =98 Hz, corresponding to D cos δ = 113 km. A more sophisticated estimator uses least squares to fit a model spectrum to the data, i.e., to extrapolate from echoes above the noise down to the spectral edges. A very simple model, corresponding to a spherical target with a $\cos^n\theta$ radar scattering law, has the form:

$$S(f) \sim \left[1 - \left(\frac{2f}{B}\right)^2\right]^{n/2} . \qquad (3)$$

Here, the spectral shape is determined by a single parameter, n, so that for non-spherical targets, the effects of target shape, orientation, and scattering properties are all absorbed by n. A correlation between B and n is "built in" to this model: echo spectra of huger. more specular targets may be difficult to distinguish from those of smaller, less *specular* ones.

Fits of an $S(f)$ model yield n = 2,.4 ± 0.7 and B = 89 ± 4 Hz. This value of B, which corresponds to $D \cos\delta$ = 102*5 km, is indicated in Fig. 10 (c), along with $B(n)$ for $1 < n \leq 6$, a range that spans values of n reported so far for fits of an $S(f)$ model to asteroid radar data, and also for modeling in which the target shape is so thoroughly parameterized that one can realistically interpret n as a measure of scattering specularity. For example. in their analysis of echo spectra of the rather elongated asteroid 1685 Toro, Ostro *et al.* (1983) obtained n = 3.6* 1.4 from fitting an $S(f)$ model spectrum to a weighted sum of 47 spectra with thorough rotation phase coverage, and n = 2.o4 ± 0.45 from fitting the entire data set with a biaxial ellipsoid model with a $\cos^n\theta$ scattering law. Also indicated in Fig. 10 (c) is the bandwidth, 110 Hz, for an equatorial view of a sphere with Zelinda's IRAS diameter. Given Zelinda's lightcurve amplitude (0.3 mag), it seems plausible that the asteroid's maximum breadth might be - 15'% larger than the IRAS diameter. We don't know if our data sample the maximum-breadth orientation, but surely we sampled orientations < 45° from it. In consideration of all this information, we conclude that our view of Zelinda was probably closer to equatorial than pole-on.

The Jan. 18 spectra exhibit a brightness feature that persists from 92.4" through 98.8" (Fig. 11), but because of a gap in phase coverage from 85" to 92°, this feature could be present at a similar strength for up to 14° of rotation phase. The bandwidth of the feature is ~12 Hz (three spectral resolution elements), corresponding to a linear dimension of at least 14 km/cm δ. As with the Iris and Metis glints, the source cannot be a reflectivity feature but rather must arise from an anomalously large fraction of the asteroid's projected area in a small Doppler domain

being normally oriented toward the radar. Even $\Delta\phi \sim 7°$ is much larger than the $\ll 1$" range that would result from a perfectly flat, kilometer-sized plane rotating through the radar-facing orientation. The observed phase-frequency signature of the radar feature probably could result from a region whose surface elements have normals within ~10° of each other. We interpret the rapid fading of the glint at 99° to mean that the responsible region is extremely flat at scales very much larger than 10 meters. Zelinda's low circular polarization ratio indicates that the surface is very smooth at cm-to-m scales.

Kleopatra

Kleopatra's maximum optical lightcurve amplitude of 1.18 magnitudes is among the largest measured for any main-belt object (Lagerkvist *et* al. 1989) and is remarkable considering the asteroid's large radiometric diameter, 135 ± 2 km. Extensive lightcurve observations have been interpreted in terms of an ellipsoidal model with axis ratios within several percent of a/b = 2.71 and b/c = 1.30 and a pole direction of either (71° ± 3°, +19° ± 3") or (236° ± 3°, +34° ± 30), with the former direction strongly favored (Magnusson 1986, 1990). Drummond et *al.* (1991) obtained axis ratios of a/b = 2.56* 0,16 and b/c = 1.33* 0.01 and a pole direction within 9" of (69", +10°), in reasonable agreement with Magnusson. A 250x90x70-km ellipsoid with Magnusson's favored pole direction would have presented the same projected area to IRAS as a 135-km-diameter sphere; however, scaling such an elongated ellipsoid to the IRAS diameter in this manner is risky (Brown 1985).

Occultation observations in 1980 and 1991 provide independent constraints on Kleopatra's dimensions. The 1980 occultation. near a time of lightcurve minimum (with $\delta \approx$ -1 50), yielded five apparently complete chords from 40 to 90 km in *length* plus four apparently incomplete chords that were fit by a 125x93 km ellipse (Dunham 1981). The 1991 occultation, near a time of lightcurve maximum (with $\delta \approx$ -34"), yielded nine apparently complete chords fit by a 230x55 km ellipse (Dunham 1992), suggesting that the asteroid is even more elongated than lightcurve-based inferences would indicate. Nevertheless, for the moment, let us adopt an ellipsoid with dimensions within 15% of 250x90x70 km and a pole direction within 3° of (71", +19°) as an *a priori* model.

The modest SNR of our Kleopatra echoes is adequate to reveal several noteworthy characteristics of the spectral signature. Figure 12 shows weighted sums of spectra in seven -45° phase intervals, The spectra from bins 4 and 7 appear to be less than half as wide as those from the other bins, which is consistent with expectations about the asteroid's extreme elongation. The shaded boxes define interval estimates of the spectral edge positions based on the *a priori* ellipsoid model. Since the phase origin of our spectra is not known accurately, we assume that the weighted average phase of the "group 4" spectrum coincides with the asteroid's minimum bandwidth orientation. Figure 13 shows two spectra obtained by taking weighted averages of the spectra from bins 4 and 7 (top panel) and from the other five bins (bottom panel). The shaded boxes in that figure correspond to the a *priori* model in its minimum and maximum bandwidth orientations. The boxes encompass the innermost zero crossings of the wide-

bandwidth spectrum but are outside those of the narrow-bandwidth spectrum. To the degree that the zero crossings approximate the true spectral edge positions, this result is consistent with the evidence from the 1991 occultation that Kleopatra's minimum pole-on breadth is shorter than that of the lightcurve-based model ellipsoid.

The most intriguing aspect of the Kleopatra echoes is the bimodality of the wide-bandwidth spectra. As shown in Fig. 12 there is a central deficit of echo power in four of the five phase groups (1, 2, 3, and 5) that exclude the narrow-bandwidth orientations. The central deficit is seen most clearly in an average of all wide-bandwidth spectra (Fig. 13, lower panel). This spectral signature, which resembles that of 4769 Castalia (Ostro *et al.* 1990), is consistent with Weidenschilling's (1980) conjecture that Kleopatra is a dumbbell-shaped asteroid, However, whereas high-SNR resolution of Castalia's echoes in time delay as well as Doppler frequency and rotation phase allowed reliable estimation of that object's shape and established its bifurcation (Hudson and Ostro 1994), our much sparser Kleopatra data set precludes shape reconstruction at a similar level of detail.

Kleopatra's weighted-mean OC radar cross section is 7100* 1800 km^2. The weighted-mean projected area of the *a priori* ellipsoid is 16200* 3400 km^2, which is 13% larger than that of a sphere with Kleopatra's radiometric diameter. (Here, weights based on the noise in each 4-minute spectrum have been applied to the projected area at corresponding phases.) Our albedo estimate based on the a priori ellipsoid is $\hat{\sigma}_{OC} = 0.44 * 0.15$. where the assigned error is intended to include systematic uncertainties in both the radar cross section and the asteroid's dimensions and orientation. Kleopatra's low "disc-integrated" circular polarization ratio ($\mu_C = 0.00 \pm 0.05$) indicates that the radar echo must arise almost entirely from single back-reflections from surface units that are smooth at cm-to-m scales, Under these circumstances. the OC radar albedo can be interpreted as the product gR of a gain factor and the Fresnel reflection coefficient at normal incidence (Eq. 1). As noted in Section 3, the gain factor g would be unity for a smooth sphere and is expected to be within a few tens of percent of unity for most large main-belt asteroids; however, Kleopatra's highly elongated shape could result in a gain factor that not only differs significantly from unity but also depends on the asteroid's orientation.

Discrepancies between Kleopatra's radar signature and predictions of the *a priori* model suggest the potential for model refinement, Limited SNR confines this study to only the simplest models that can account for the spectra, but perhaps the most important benefit of this approach is that in modeling the echoes, one can estimate the average scattering law as well as the shape. In this way, the shape model accounts for structural contributions to g at "tile" scales, while the scattering law absorbs contributions tog from structure at smaller ("facet'? scales. This mitigates a significant source of uncertainty in the interpretation of Kleopatra's radar albedo.

A simple four-parameter model for Kleopatra consists of a biaxial ellipsoid ($a \geq b = c$) *with* a $\rho \cdot \cos^n\theta$ scattering law. The model's scale (in km) is uncertain by at least ~20% because of uncertainty in the pole direction; however, the scale factor cancels in the ratio *a/b*. As before, we assume that the weighted average phase of the "group 4" spectrum in Fig. 12 coincides with the asteroid's minimum bandwidth orientation. This has the effect of minimizing estimates for the *a/b* ratio. Figure 14 shows the least-squares result, which yields a reduced chi-square of 1.10. The

expected correlation between the ellipsoid's dimensions and the scattering law exponent was evident in our search for the best-fit values of a, b, p, and n; however, our estimate for this model's a/b ratio, 4.1 ± 1.3 (95% confidence), supports the hypothesis that Kleopatra is more elongated than lightcurve-based estimates.

Two biaxial ellipsoids in contact provide a slightly more complicated model, with three additional free parameters: two for the second ellipsoid's axes and one for the separation of the ellipsoids' centers. (The ellipsoids are allowed to overlap, but the a-axes are forced to be collinear. in addition, the Doppler frequency of the model's center of mass is forced to coincide with the prediction ephemeris.) Figure 15 shows the least-squares result, which has a reduced chi-square of 0.98. The -10% improvement in χ^2 supports the hypothesis that the two-ellipsoid model provides a better fit to the data than does the one-ellipsoid model. The breadth ratio, defined to be the model's total extent along the line containing the a-axes divided by the maximum extent orthogonal to that line, is 3.6 ± 1.1 (95% confidence). This supports our favored hypothesis that Kleopatra is more elongated than lightcurve-based estimates but does not rule out a breadth ratio as small as -2.5.

The one- and two- component ellipsoid models provide acceptable fits to the data, but the 1991 occultation chords (Fig. 16) suggest that both models are simplistic. Those chords, albeit few, show no evidence for a bifurcated shape. On the contrary, one anomalously long chord hints at the presence of a 25-km-high "mountain" (Dunham 1992). Extensive explorations of more complex shapes indicate that a variety of nonconvex shapes can provide good visual matches to our spectra but cannot survive statistical tests of significance — the SNR and geometric leverage of our data simply are inadequate. In light of the 1991 occultation, we cannot rule out the possibility that the bimodal spectra arise from radar reflectivity variations along the length of the asteroid.

Regardless of whether or not Kleopatra is bifurcated, the ellipsoid models provide insight into the physical interpretation of Kleopatra's radar albedo. It is useful to define the "equivalent spherical albedo" ($\hat{\sigma}_S$) to be the radar albedo that a sphere would have for any particular scattering law (Hudson and Ostro 1994). The goal here is to separate the contribution of Kleopatra's overall shape (at "tile" scales and larger) from the gain factor g, which may permit more useful comparisons with other radar-detected MB As, whose shapes are generally less exotic than Kleopatra's. For the cosine scattering law used above, $\hat{\sigma}_S = 2\rho/(n+1)$. The equivalent spherical albedo of the one-ellipsoid model is $\hat{\sigma}_S$ =0.52*0.21. and that of the two-ellipsoid model is $\hat{\sigma}_S$ =0.50*0.19. Both estimates are similar to $\hat{\sigma}_{OC}$ (the albedo based on the *a priori* ellipsoid), which shows that Kleopatra's elongation need *not* result in a value of g significantly different from unity. On this basis, we expect physical inferences from comparison of Kleopatra's albedo with other MBA values to be reliable. Furthermore, if we assume that surface structures at "facet" scales can be treated statistically as a distribution of slopes, and if we adopt Parker's (1973) slope probability density function. then for a sphere with a $\rho \cdot \cos^n\theta$ scattering law we can write: $g = 1 + s_0^2/(1+s_0^2)$, where $s_0 = \sqrt{2/n}$ *is the* adirectional rms slope (see the Appendix). For $n \sim 6$, facet-scale surface structures increase a sphere's gain factor g by only ~ 14%. Thus, we expect Kleopatra's radar albedo ($\hat{\sigma}_{OC}$) to be a reasonable first approximation to R. We will return to this issue in Section 5.

Victoria

Victoria's lightcurves have a (synodic) period of 8.662 hours (Erikson 1990) and a maximum amplitude of -0.3 mag (Lagerkvist *et al.* 1989), similar to lightcurve amplitudes for Iris and Zelinda. No lightcurve-based shape model has been published, but Tempesti and Burchi (1969) estimated the pole direction to be (RA, Dec) = ($4^h12^m \pm$ 6"', +3"* 30), noting that their quoted uncertainty is probably too small. The corresponding ecliptic coordinates are $\lambda = 242° \pm 3"$ and $\beta = +17° \pm 4"$. Victoria's radiometric diameter is 113 ± 3 km (Tedesco and Veeder 1992).

Victoria's sky positions during our 1982 and 1989 observations were -30° apart. Figure 17 shows weighted sums of spectra for each apparition. The above pole direction predicts subradar latitudes of -30" ± 5" in 1982 and -2" ± 4° in 1989. From Eq. 2, the instantaneous bandwidth (B, Hz) and breadth (D, km) satisfy: $B(D) = 3.20\ D \cos\delta$. For a maximum pole-on breadth between 1.0 and 1.2 times the radiometric diameter. the predictions for δ correspond respectively to B = 290-400 Hz and 350-440 Hz, as indicated by the brackets in Fig. 17. The zero crossing bandwidths in 1982 and 1989 are significantly smaller than the predicted values. .

As with Zelinda, we have used least-squares fits of an $S(f)$ spectral model (Eq. 3) to constrain B and hence δ. The shaded boxes in Fig. 17 show spectral edge positions from fits with n fixed to values between 1 and 6. Figure 18 shows constraints on Victoria's pole direction based on our $S(f)$ band width estimates and the assumption that the maximum breadth sampled in each year was within 20% of 113 km. For each year, our interval estimate for δ defines an annular domain of possible pole directions (dotted curves). The intersection of the domains from 1982 and 1989, outlined by the thick curves, bound the space of admissible pole directions. If we instead enforce the predicted bandwidths on the $S(f)$ model, then fits to our spectra yield n = 7.3 (12.8) for the 1982 (1989) observations. It is, of course, conceivable that an exotic shape *and* an unusually specular scattering law have conspired to produce spectra for which any of our bandwidth estimation approaches would lead to a gross underestimate of B; however, to the extent that our experience with the other targets discussed here is a valid guide, we prefer the hypothesis that in each year δ was significantly *huger than the* Tempesti-Burchi predictions.

Figures 19 and 20 show weighted sums of spectra within -50" phase intervals (a) and ~8° phase intervals (b) from the 1982 and 1989 observations, respectively. Figure 20 shows that the 1989 spectra are persistently bimodal throughout the third phase interval, but are unimodal throughout the opposite (first) interval. This pattern is also evident in the somewhat noisier 1982 echoes (Fig. 19), but the rotation period is not known with sufficient accuracy to provide a common phase origin for both data sets. Instead, we have numbered each of the 1989 phase groups to match the most nearly corresponding 1982 phase group based on the qualitative appearance of the spectra.

We have explored the character of irregular shapes that can produce model spectra with Victoria's unusual spectral signature; however, such models demand large numbers of shape parameters, precluding identification of a statistically acceptable, demonstrably unique model. To the extent that the backscattering is uniform and geometric

$(\sigma_o(\theta) - \cos\theta)$, a Doppler spectrum maps the distribution of projected area across the object's plane-of-sky projection. An axisymmetric object spinning about a symmetry axis would give identical spectra at all phases. (Let us assume principal-axis rotation throughout this discussion.) For a geometrically scattering target viewed equatorially, echo spectra 180" apart would be identical but with the Doppler frequency reversed. These extreme examples clearly do not apply to Victoria. Rather, the asteroid's distinctive signature must involve some interesting shape and/or scattering properties. In light of (i) the persistence in phase of the spectral bifurcation, (ii) the apparently modest limb-darkening of MBAs at radar wavelengths, and (iii) the absence of observational evidence for (or theoretical arguments predicting) severe radar albedo variations on S-class MBAs, we expect that the object would have a strongly bimodal appearance in t-he orientation that produced our bimodal spectra. That is, we suggest that the simplest hypothesis is that Victoria's strongly bimodal spectra most likely arise from a prominent concavity. Since opposite phases are not bimodal, we infer that the shape is not axisymmetric and that our view was at least a few tens of degrees from equatorial (consistent with the radar constraints on pole direction).

5. RAM1FJCATIONS FOR INDIVIDUAL OBJECTS AND ASTEROID SCIENCE

Disk-integrated properties

Table III lists for each experiment our estimates of the OC radar cross section. circular polarization ratio, and OC radar albedo, which were determined from weighted averages of all available spectra. For Iris, Metis, and Victoria, there is reasonable agreement in $\hat{\sigma}_{OC}$ from year to year once expected variations in projected area are accounted for, The circular polarization ratios for each target also show good agreement, except for Iris. as noted in Section *4*. Table IV lists for each target the weighted averages of μ_C and $\hat{\sigma}_{OC}$ from all Arecibo observations. The low circular polarization ratios indicate that most of the echo power arises from single back-reflections from smooth surface elements. so that $\hat{\sigma}_{OC} = gR$ may be used to constrain the normal reflectivity /?. As discussed by 0CS85 and Ostro *et al. (1991),* for dry, particulate mixtures of meteoritic minerals with particle sizes no *larger than* -2./100, *R* depends almost linearly on bulk density (d), which in turn is a function of the pore fraction (porosity) and the zero-porosity density (the specific gravity) of the mixture's solid material. An empirical relation (Garvin *et al.* 1985) that is applicable for porosities higher than ~20% is:

$$d(R) = 3.2 \ln \frac{1 + \sqrt{R}}{1 - \sqrt{R}} \qquad (4)$$

For mixtures of metal and silicates with porosities lower than about 20%, small volume concentrations of metal can increase *R* by an amount that depends on the electrical properties of each phase and on the metal particles' dimensions and packing geometry, For solid enstatite chondrites, whose typical density corresponds to a reflectivity of 0.26 by the above formula, laboratory investigations of "loaded dielectrics" predict reflectivities between 0.4 and 0.7 and measurements of meteorite specimens yield values ~ 0.7 (Fig.21 [b]).

Figure 21 (a) plots the OC radar albedos of most radar-detected MB As. When taken as a group, so as to average out target-to-target variations in g, S-class MBAs tend to have somewhat higher radar albedos than C-class MBAs. This is consistent with expectations about mineralogical differences between S- and C-class asteroids (Table V). The radar albedos of Iris and Metis are *typical* of radar-detected, S-class MBAs, which have an unweighed mean radar albedo of 0.14*0.04 (0(S85). In contrast, Victoria has the highest radar albedo yet measured for an S-class MBA. Similarly, Zelinda's radar albedo is higher than most other C-class radar targets, which have an unweighed mean radar albedo of 0.11 ± 0.04. Differences in $\hat{\sigma}_{OC}$ among our three S-class targets and between Zelinda and C-class targets as a group could be due to variations in surface mineralogy (e.g.. Gaffey *et al.* 1993), surface porosity, and regolith thickness; however, in the absence of detailed shape information, physical inferences based on the radar albedo of any individual target are obscured by uncertain y in g, especially in the case of Victoria, which evidently has a very unusual shape.

Kleopatra's radar albedo exceeds those of all other radar-detected MBAs (the next highest is 0.28 for 16 Psyche) and all radar-detected NEAs except 1986 DA ($\hat{\sigma}_{OC}$ = 0.58; Ostro *et* al. 1991). Moreover, the asteroid's near-zero value of μ_c distinguishes Kleopatra as one of the smoothest radar-detected targets at cm-to-m scales. Candidate meteorite analogs for M asteroids are irons (possibly with silicate inclusions) and enstatite chondrites, which are assemblages of NiFe metal and enstatite (Table V). With the above formula, a reflection coefficient equal to Kleopatra's albedo corresponds to densities between 3.8 and 6.5 g cm^{-3}. Taken at face value, these numbers are consistent with a nearly entirely metallic composition and a porosity typical of the lunar regolith (-40%), but rule out an enstatite chondrite mineralogy unless the porosity is nearly zero. (Note that for any given porosity, R is two to three times higher for irons than for enstatite chondrites.) The equivalent spherical albedos derived in Section 4 argue that Kleopatra's high radar albedo is not simply an artifact of a highly elongated shape. Thus, unless the asteroid is unusual in some other respect (e.g., if the regolith thickness were $\ll$ 1 m on Kleopatra but >>1 m on other radar-detected asteroids), it might be a core remnant of a collisionally disrupted. differentiated asteroid.

Shapes

Collisions are believed to be the dominant geologic process in the asteroid belt. Catastrophic impacts provide a natural explanation for asteroid families (Chapman *et* al. 1989), but serious questions remain about the extrapolation of laboratory impact experiments over many orders of magnitude to asteroid sizes and the extents to which internal material strength and self gravity play a role as a function of size (Fujiwara *et al.* 1989 and references therein, Heusen *et al.* 1991, Ryan *et al. 1991,* Nakamura *et a/.* 1992). Nevertheless, the shape distribution of fragments produced in laboratory impact experiments closely resembles that of moderate to small (D < 100 km) main-belt asteroids as inferred from their lightcurves (Capaccioni *et al. 1984).* Larger asteroids tend to have smaller lightcurve amplitudes and are thought to have more symmetrical shapes. Based on inferred collision rates in the main belt, large asteroids ($D \gtrsim$ 150 km) are thought to be thoroughly fractured by collisions (Farinella et *al.* 1982, Davis et *al.* 1989), possibly resulting in zero-strength "rubble piles" with shapes governed largely by the influences of gravity

and centrifugal force (Weidenschilling 1980). However, little is known about the internal structures of MBAs, e g,, the size distribution of the inferred rubble and how internal structures might be manifested at the surface. An asteroid's ability to reach an ideal equilibrium shape (e.g.. a Maclaurin spheroid or a Jacobi ellipsoid) could be limited by the largest rubble fragments.

Galileo images of Gaspra and Ida reveal concavities and flat regions spanning significant fractions of those asteroids' dimensions (Thomas et *al.*1994, Belton *et al.* 1994). One of the flat regions on Gaspra is 6 km across, or roughly one third of asteroid's longest dimension. Stereographic measurements show that the maximum deviation from a plane in that region is 0.21 km. A preliminary analysis of Ida images reveals similar planar regions on an asteroid two times larger (Belton *et al.* 1994). The origin of these flat regions is currently unknown, although Greenberg *et al. (1994)* suggest that these regions and others could be of impact origin. In any event. such topography suggests the presence of coherent structures (possibly "blocks" with significant tensile strength). Moore et *al.* (1994) suggest that stress-wave focusing could be responsible for grooved terrain on Ida, which would imply that the bulk of Ida is a single coherent structure.

Radar spikes in our spectra of Iris, Metis, and Zelinda suggest that large flat regions exist on asteroids much larger than Gaspra and Ida — indeed, the flat regions themselves appear to be larger than Gaspra. Are such features common on asteroid surfaces? The fact that glints were. observed from 3 of the 37 radar-detected MBAs may be significant considering the ~ 10% probability of any particular flat region being oriented within 10° of the radar-facing direction at some time during an observation with complete rotational coverage. Future observations (see below) are expected to provide a much larger and higher SNR asteroid radar sample. The prevalence of flat regions, especially if they attest to the presence of blocks, may improve our understanding of the internal structures of MBAs.

Radar spectra of Kleopatra and Victoria suggest that the shapes of large MBAs can be far removed from simple ellipsoids, but the available information leaves us with more questions than answers. Kleopatra is by all accounts highly elongated, but it is unclear whether the asteroid is a "contact binary" or a single component with a prominent concavity, or if strong radar reflectivity variations along the asteroid's length have conspired to produce the bimodal radar spectra. Victoria's unusual radar signature implies the presence of a prominent concavity, but the asteroid's gross shape remains largely unknown. We note that the amplitudes and shapes of Victoria's lightcurves are unremarkable (Lagerkvist *et al.* 1987, 1988; Binzel *et al* 1989), which raises the question of what fraction of large MBAs possess large-scale topography and serves as a reminder of the limitations of triaxial ellipsoids as approximations to asteroid shapes.

6. FUTURE OBSERVATIONS

Our ability to constrain the shapes of Kleopatra and Victoria and the surface mineralogy of any of our targets was limited by the available SNR and the lack of delay-resolved echoes, which provide important geometric leverage for the shape inversion technique described above. This situation is expected to improve dramatically in mid- 1996 upon completion of a major upgrade of the Arecibo telescope, which should provide a -20-fold increase in radar sensitivity (Campbell et *al.* 1994). Table VI lists OC SNR predictions for selected opportunities between 1997 and 2007 to observe our five targets with the upgraded Arecibo radar. (For comparison, the peak SNR per day was -2000 during the 1989 observations of Castalia.) These are by no means the only MBA opportunities –- roughly five per year will have SNR > 100 per day. An experiment spanning several days on such a target would provide enough echo strength to place 100's of delay-Doppler cells on the asteroid at each of many different rotation phases. Such data sets may be inverted to provide simultaneous estimates of the target's three-dimensional shape and radar scattering properties with the same techniques used for Castalia, thus enabling us to place useful constraints on MBA mineralogy and potential meteoritic associations.

APPENDIX

Under the assumptions of geometric optics (facet ≫ wavelength; μ_C = O) and perfect conductivity (R = 1), Simpson and Tyler (1982) derive an expression for the radar cross section per unit surface area on the target:

$$\sigma_0 = \frac{d\sigma}{dA} = \frac{\sec\theta}{2} p_P(\theta) \tag{A-1}$$

where $p_P(\theta)$ is the probability that a facet's normal is within a solid angle dω making an angle θ with respect to the mean surface normal (Parker 1973). This probability density function is normalized via:

$$\int_0^{\pi/2} p_P(\theta) \sin\theta \, d\theta = 1 \ , \tag{A-2}$$

To relate Eq. A-1 to the empirical *"cosine"* scattering law ($\sigma_0 = p \cos^n\theta$) introduced in Section 3 and utilized in our modeling of Kleopatra echoes, we first relax the assumption of perfect conductivity by multiplying the right hand side of Eq. A-1 by the Fresnel reflection coefficient at normal incidence, R. Then. combining the cosine scattering law with Eqs. A-1 and A-2 yields:

$$p_P(\theta) = (n + 2) \cos^{n+1}\theta \tag{A-3}$$

and

$$R = \frac{2p}{n+2} \ . \tag{A-4}$$

Given the slope probability density function, $p_P(\theta)$, the adirectional rms slope (s_o) can be calculated via (Simpson and Tyler 1982):

$$s_o = \left(\tan^2\theta_{rms} \right)^{1/2} = \left[\int_0^{\pi/2} \tan^2\theta \, p_P(\theta) \sin\theta \, d\theta \right]^{1/2} = \sqrt{2/n} \ . \qquad \text{(A-5)}$$

Equations A-1 through A-5 apply at the tile scale. that is, the shape has not yet been specified. As a concrete example, the radar cross section of a sphere with a diameter D and a cosine scattering law is:

$$\sigma_S = \int \frac{d\sigma}{dA} \cdot dA = \int_0^{\pi/2} (\rho \cos^n\theta) \cdot \frac{\pi D^2}{2} \sin\theta \, d\theta = \frac{\pi D^2 \rho}{2(n+1)} \ , \qquad \text{(A-6)}$$

which corresponds to a radar albedo of

$$\hat{\sigma}_S = \frac{4\sigma_S}{\pi D^2} = \frac{2\rho}{n+1} = \frac{n+2}{n+1} R \ . \qquad \text{(A-7)}$$

Finally, the sphere's gain factor g is:

$$g = \frac{\hat{\sigma}_S}{R} = \frac{n+2}{n+1} = 1 + s_o^2/(1+s_o^2) \ . \qquad \text{(A-8)}$$

ACKNOWLEDGMENTS

We thank the staff of the Arecibo Observatory and the Goldstone Radio AstronomyRadar Group for assistance with the observations. Part of this research was conducted at the Jet Propulsion Laboratory, California Institute of Technology, under contract with the National Aeronautics and Space Administration (NASA). Work at the Center for Astrophysics was supported in part by NASA. DLM is a Research Associate of the National Research Council. The Arecibo Observatory is part of the National Astronomy and Ionosphere Center, which is operated by the Cornell University under a cooperative agreement with the national Science Foundation and with support from NASA.

REFERENCES

BARRUCI, M. A., M. FULCHIGNONI, AND V. ZAPPALÁ 1984. On the estimate of the shape of regular asteroids. *BAAS* **16,700.**

BROWN, R. H. 1985. Ellipsoidal geometry in asteroid thermal models: The standard radiometric model, *Icarus* **64,** 53-63.

BELTON, M. J. S., C. R. CHAPMAN, J. VEVERKA, K. P. KLAASEN, A. HARCH, R. GREELEY, R. GREENBERG, J. W. HEAD HI. A. MCEWEN, D. MORRISON, P. C. THOMAS. M, E. DAVIES, M. H. CARR, G. NEUKUM, F. P. FANALE, D. R. DAVIS, C. ANGER, P. J. GIERASCH, A. P. INGERSOLL., AND C. B. PILCHER]994. First images of asteroid 243 Ida. *Science* **265.1543-1547.**

BINZEL, R. P., P. FARINELLA, V. ZAPPALÁ, AND A. CELLINO 1989. Asteroid rotation rates: Distributions and statistics. In *Asteroids II* (R. P. Binzel, T. Gehrels, and M. S. Matthews, Eds.) pp. 416-441. Univ. of Arizona Press, Tucson.

BINZEL, R. P., S. M. SLIVAN, P. MAGNUSSON, W. Z. WISNIEWSKI, J. DRUMMOND, K. LUMME, M. A. BARUCCI, E. DOTTO, C. ANGELI, D. LAZZARO, S. MOTTOLA, M. GONANO-BEURER, T. MICHALOWSKI, G. DE ANGELIS, D. J. THOLEN, M. DI MARTINO, M. HOFFMANN, E. H. GEYER, AND F. VELICHKO 1993. Asteroid 243 Ida: Groundbased photometry and a pre-Galileo physical model. *Icarus* **105**, *310-325.*

BUCHWALD, V. F. 1975. *Handbook of Iron Meteorites, pg. 86.* Univ. of California Press, Berkeley

CAMPBELL, D. B., G. J. BLACK, AND *S.* J. OSTRO 1994. Asteroids and comets: Future imaging opportunities with Earth-based radar systems. *BAAS* **26,** 1167.

CAMPBELL, M. J., AND J. ULRICHS 1969, Electrical properties of rocks and their significance for lunar radar observations. *J. Geophys. Res. 74,5867-5881.*

CAPACCIONI, F., P. CERRONI, M. CORADINI, P. FARINELLA, E. FLAMINI, P. HURREN, G. MARTELLI, AND P. N. SMITH *1984.* Shapes of asteroids compared with fragments from hypervelocity impact experiments. *Nature* **308,832-***834.*

CHAPMAN, C. R.. P. PAOLICCHI, V. ZAPPALA, R. P. BINZEL, AND J. F. BELL 1989. Asteroid families: Physical properties and evolution, In *Asteroids II* (R. P. Binzel, T. Gehrels, and *M. S.* Matthews, Eds.) pp. 386-415. Univ. of Arizona Press, Tucson.

DAVIS, D. R., S. J. WEIDENSCHILLING, P. FARINELLA, P. PAOLICCHI, AND R. P. BINZEL 1989, Asteroid collisional history: Effects on sizes and spins. In *Asteroids II* (R. P. Binzel, T. Gehrels, and M. S. Matthews, Eds.) pp. 805-826. Univ. of Arizona Press, Tucson.

DE PATER, I., P. PALMER, D. L. MITCHELL, *S.* J. OSTRO, D. K. YEOMANS, AND L. E. SNYDER 1994. Radar aperture synthesis observations of asteroids, *Icarus* **111,489-502.**

DODD, R. T., *1981. Meteorites.* Cambridge Univ. Press. Cambridge,

DRUMMOND, J. D., AND E. K. HEGE 1989. Speckle interferometry of asteroids. In *Asteroids II* (R. P. Binzel, T. Gehrels, and M. S. Matthews, Eds.) pp. 171-191. Univ. of Arizona Press, Tucson.

DRUMMOND, J. D., S. J. WEIDENSCHILLING, C. R. CHAPMAN, AND D. R. DAVIS 1991. Photometric geodesy of main-belt asteroids. IV. An updated analysis of lightcurves for poles, periods, and shapes. *Icarus* **89,44-64.**

DUNHAM, D. W. 1981. Recently-observed planetary occultations. *occultation Newsletter* **2** (1 1), 139-143.

DUNHAM, D. W, 1992. Planetary occultations of stars in 1992. *Sky & Telescope,* January 1992, pp. 72-73.

ERIKSON, A. 1990. Improvement of rotation periods for the asteroids 12 Victoria, 173 Ino and 1245 Calvinia. In *Asteroids, Meteors, and Comets III* (C.-I. Lagerkvist, H. Rickman, B. A. Lindblad, and M. Lindgren, Eds.), pp. 55-58. Uppsala University, Sweden.

FARINELLA, P., P. PAOLICCHI, AND V. ZAPPALÀ 1982. The asteroids as outcomes of catastrophic collisions. *Icarus 52, 409-433.*

FUJIWARA, A.. P, CERRONI, D. DAVIS, E. RYAN. M. DI MARTINO, K. HOLSAPPLE, AND K. HOUSEN 1989. Experiments and scaling laws for catastrophic collisions. In *Asteroids II (R.* P. Binzel, T. Gehrels, and M. S. Matthews, Eds.), pp. 240-265. Univ. of Arizona Press, Tucson,

GAFFEY, M. J., J. F. BELL, R. H. BROWN, T. H. BURBINE, J. L. PIATEK, K. L. REED, AH'D D. A. CHAKY 1993. Mineralogical variations within the S-type asteroid class. *Icarus* **106,573-602.**

GARVIN, J. B., J. W. HEAD, G. H. PETTENGILL, S. H. ZISK 1985. Venus global radar reflectivity and correlations with elevation. *J. Geophys. Res. 90.6859-6871.*

GLASS, B. P. 1982. *Introduction to Planetary Geology.* Cambridge Univ. Press, Cambridge.

GREENBERG, R., M, C. NOLAN, W. F. BOTTKE, JR., R. A. KOLVOORD, AND J. VEVERKA 1994. Collisional history of Gaspra. *Icarus 107,84-97.*

HOUSEN, K. R., R. M. SCHMIDT, AND K. A. HOLSAPPLE 1991. Laboratory simulations of large scale fragmentation events, *Icarus* **94**, 180-190.

HUDSON, S. 1993. Three-dimensional reconstruction of asteroids from radar observations. *Remote Sensing Reviews 8,* 195-203.

HUDSON, R. S., AND S, J. OSTRO 1994. Shape of asteroid 4769 Castalia (1989 PB) from inversion of radar images. *Science* **263,940-943.**

KEIL, K. 1%8. Mineralogical and chemical relationships among enstatite chondrites. *J. Geophys. Res.* **73**, 6945-6976.

KELLY, J. M., J. O. STENOIEN, AND D. E. ISBELL 1953. Wave-guide measurements in the microwave region on metal powders suspended in paraffin wax. *J. Appl. Phys. 24,258--262.*

KRISTENSEN, L. K. 1984. (9) Metis okkultationen den 19 februar 1984. *Astronomi & Rumfart* Maj-Jun 1984, pp. 76-78,

LAGERKVIST, C. -I., M. A. BARUCCI, M. T. CAPRIA, M. FULCHIGNONI, L. GUERRIERO, E. PEROZZI, AND V. ZAPPALA 1987. *Asteroid Photometric Catalog* (Consiglio Nazionale delle Ricerche, Rome, Italy).

LAGERKVIST, C. -I., M. A. BARUCCI, M. T. CAPRIA, M. FULCHIGNONI, P. MAGNUSSON, AND V. ZAPPALÀ 1988. *Asteroid Photometric Catalog (First Update)* (Consiglio Nazionale delle Ricerche, Rome, Italy).

LAGERKVIST, C. -I., A. W. HARRIS, AND V. ZAPPALA 1989. Asteroid Lightcurve Parameters. In *Asteroids II* (R. P. Binzel, T. Gehrels, and M. S. Matthews, Eds.), pp. 1162-1179. Univ. of Arizona Press, Tucson,

LEBOFSKY, L. A., AND J. R. SPENCER 1989. Radiometry and thermal modeling of asteroids. In *Asteroids II* (R. P. Binzel, T. Gehrels, and M. S. Matthews. Eds.), pp. 128-147. Univ. of Arizona Press. Tucson.

LIPSCHUTZ, M. E., M. J. GAFFEY, AND P. PELLAS 1989. Meteoritic parent bodies: Nature, number, size and relation to present-day asteroids. In *Asteroids II (R.* P. Binzel, T. Gehrels, and M. S. Matthews, Eds.), pp. 740-777. Univ. of Arizona Press. Tucson.

MAGNUSSON, P. 1986. Distribution of spin axes and senses of rotation for 20 large asteroids. *Icarus 68, 1-39.*

MAGNUSSON, P., M. A. BARUCCI, J. D. DRUMMOND, K. LUMME, S. J. OSTRO, J. SURDEJ, R. C. TAYLOR, AND V. ZAPPALA 1989. Determination of pole orientations and shapes of asteroids. In *Asteroids II* (R. P. Binzel, T. Gehrels, and M. S. Matthews, Eds.), pp. 66-97. Univ. of Arizona Press, Tucson,

MAGNUSSON, P. 1990. Spin vectors of 22 large asteroids. *Icarus 85,229-240.*

MAGNUSSON, P., M. A. BARUCCI, R. P. BINZEL, C. BLANCO, M. DI MARTINO, J. D. GOLDADER, M. GONANO-BEUER, A. W. HARRIS, T. MICHALOWSKI, S. MOTTOLA, D. J. THOLEN, AND W. Z. WISNIEWSKI 1992. Asteroid 951 Gaspra: Pre-Galileo physical model. *Icarus* 97, 124-129.

MCCARTHY, D. W., JR., J. D. FREEMAN, AND J. D. DRUMMOND 1994. High resolution images of Vesta at 1.65 μm. *Icarus 108,285-297.*

MCFADDEN, L, A., D. J. THOLEN, AND G. J. VEEDER 1989. Physical properties of Aten, Apollo and Amor asteroids. In *Asteroids II* (R. P. Binzel, T. Gehrels, and M. S. Matthews, Eels.), pp. 442-467. Univ. of Arizona Press, Tucson.

MILLIS, R. L., AND D. W. DUNHAM 1989. Precise measurement of asteroid sizes and shapes from occultations. In *Asteroids II* (R. P. Binzel, T. Gehrels, and M. S. Matthews, Eds.), pp. 148-170. Univ. of Arizona Press, Tucson.

MOORE, J. M., E. ASPHAUG, D. MORRISON, AND THE GALILEO IMAGING TEAM (1994). Ida collisional history I: Stress-wave focusing as an explanation for grooved terrain, *BAAS 26* (No. 3), 1157.

NAKAMURA, A.. K. SUGUIYAMA, AND A. FUJIWARA 1992. Velocity and spin of fragments from impact disruptions: An experimental approach to a general law between mass and velocity. *Icarus* **100**, 127-135.

NIELSEN, L. E. 1974. The permittivity of suspensions and two-phase mixtures. *J. Phys. D: Appl. Phys.* **7**, *1549-1554.*

OSTRO, S. J., D. B. CAMPBELL, AND I. I. SHAPIRO 1983. Radar observations of asteroid 1685 Toro. *Astron. J.* **88,** S65-576.

OSTRO, S. J., D. B. CAMPBELL, AND I. I. SHAPIRO 1985. Mainbelt asteroids: dual-polarization radar observations. Science **229,442-446.**

OSTRO, S. J., K. D. ROSEMA, AND R. F. JURGENS 1990. The shape of Eros. *Icarus* **84,334-351.**

OSTRO, S. J., D. B. CAMPBELL, J. F. CHANDLER, A. A. HINE, R. S. HUDSON, K. D. ROSEMA, AND I. I. SHAPIRO 1991. Asteroid 1986 DA: Radar evidence for a metallic composition *Science 252, 1399-1404.*

OSTRO, S. J., D. B. CAMPBELL, R. A. SIMPSON, R. S. HUDSON, J. F. CHANDLER, K. D. ROSEMA, L L SHAPIRO, E. M. STANDISH, R. WINKLER, D. K. YEOMANS, R. VELEZ, AND R. M. GOLDSTEIN 1992. Europa, Ganymede, and Callisto: New radar results from Arecibo and Goldstone. *J. Geophys. Res.* 97, 18227-18244.

PARKER, M. N, 1973. Radio-wave scattering from rough surfaces and the estimation of surface shape. Ph. D. dissertation, Stanford University. Stanford, CA.

PETTENGILL, G. H., P. G. FORD, AND B. D. CHAPMAN 1988. Venus: Surface electromagnetic properties. *J. Geophys. Res. 93.14881-14892.*

RYAN. E. V., W. K. HARTMANN, AND D. R. DAVIS 1991. Impact experiments 3: Catastrophic fragmentation of aggregate targets and relation to asteroids. *Icarus 94,283-298.*

SAINT PÉ, O., M. COMBES, E RIGAUT, M. TOMASKO, AND M. FULCHIGNONI 1993a. Demonstration of adaptive optics for resolved imagery of solar system objects: Preliminary results on Pallas and Titan. *Icarus 105,263-270.*

SAINT PÉ, O., M. COMBES, AND F. RIGAUT 1993b. Ceres surface properties by high-resolution imaging from Earth. *Icarus 105,271-281.*

SCHOBER, H. J. 1975. The minor planet 654 Zelinda: Rotation period and light curve. *Astron. Astrophys. 44,85-89.*

SIMPSON. R. A., AND G. L. TYLER 1982. Radar scattering laws for the lunar surface. *IEEE Trans. on Antennas and Propagation* **AP-30**, No. *3,438449.*

TEDESCO, E. F., AND G. J. VEEDER 1992. In *IRAS Minor Planet Survey (E.* F. Tedesco, Ed.), pp. 243-285. Phillips Laboratory Technical Report No. PL-TR-92-2049, Hanscom Air Force Base, MA.

TEMPESTI, P., AND R. BURCHI 1969. A photometric research on the minor planet 12 Victoria. *Mem. Sot. A.wren. Italiana 40,415-432.*

THOLEN, D. J. 1989. In *Asteroids II* (R. P. Binzel, T. Gehrels, and M. S. Matthews, Eds.), pp. 1139-1150, Univ. of Arizona Press, Tucson.

THOMAS, P. C., J. VEVERKA, D. P. SIMONELLI, P. HELFENSTEIN, B. CARCICH, M. J. S. BELTON, M. E. DAVIES, AND C. CHAPMAN 1994. The shape of Gaspra. *Icarus 10'7,23-36.*

TIURI, M. E. 1964. Radio astronomy receivers. *IEEE Trans. Antennas Propag.* **AP- 12,930-938**

TSVETKOVA, V. S., V. N. DUDINOV, S. B. NOVIKOV, YE. A. PLUZHNIK, YU. G. SHKURATOV, V. G. VAKULIK, AND A. P. ZHELEZNYAK 1991. Shape and size of asteroid 4 Vesta: Speckle interferometry and polarimetry. *Icarus* **92, 342-349.**

ULABY, F. T., T. H. BENGAL, M. C. DOBSON, J. R. EAST, J. B. GARVIN, ANI) D. L. EVANS 1990. Microwave dielectric properties of dry rocks. *IEEE Trans. Geosci. Remote Sensing 28,325-336.*

WEIDENSCHILLING, S. J. 1980, Hektor: Nature and origin of a binary asteroid. *Icarus* 44,807-809.

ZAPPALÀ, V., AND Z. Knežević 1984. Rotation axes of asteroids: Results for 14 objects. *Icarus 59.436455.*

ZAPPALÀ, V., AND M. DIMARTINO 1986. Rotation axes of asteroids via the amplitude-magnitude method: Results for 10 objects. *Icarus 68,40-54.*

Table I : Observations

Target	Dates Spanned (UT)	t_0 (h, UT)	# runs	RA (h)	Dec (deg)	Dist (AU)	f_{TX} (MHz)	Af (Hz)
7 Iris	1980 Sep 26 - Ott 01	2.62	7	23.6 (0.07)	10 (0.6)	0.94 (0.001)	2380	9.8
	1984 Dec 19- Dec 24	2.84	25	5.3 (0.08)	22 (0.5)	0.95 (0.018)	"	9.8
	1991 Sep 15 - Sep 28	4.43	32	22.7 (0.17)	3 (1)	1.02 (0.012)	8495	39.1
9 Metis	1984 Mar 17- Mar 22	3.39	15	12.2 (0.03)	9 (0.4)	1.44 (0.006)	2380	9.8
	1986 Nov21 - Nov 23	2.25	9	4.4 (0.04)	21 (0.04)	1.12 (0.003)	"	9.8
12 Victoria	1982 Sep 29 - Oct 05	1.16	15	0.2 (0.08)	15 (1.1)	1.03 (0.014)	"	9.8
	1989 Aug 19- Aug 21	8.62	9	22.3 (0.03)	9 (0.1)	0.88 (0.001)	"	9.8
216 Kleopatra	1985 Nov 18- Dec 01	0.21	13	4.0 (O. 16)	9 (2.0)	1.18 (0.024)	"	18.8
654 Zelinda	1988 Jan 17 – Jan 18	6.70	9	5.7 (0.01)	21 (0.3)	0.89 (0.004)	"	3.9

Table I: Right ascension, declination, and distance are given for epochs near the weighted midpoint of observation; the range of values spanned is in parentheses. An epoch of zero rotation phase, t_0, is given for the first date of each experiment. Zero phase does not correspond to any particular orientation of the asteroid, nor is there any phase correspondence from year to year. The number of transmit-receive cycles, or runs, is given in the fourth column. The transmitter frequency (f_{TX}) and the raw frequency resolution (Δf) of the echo Doppler spectra are given in the last two columns.

Table II : Prior Information

Target	(1) Class	(2) IRAS Diameter	(3) Model Ellipsoid 2a	2b	2c	(4) Synodic Period	(5) Pole Direction long.	lat.	(6) Year	(7) δ	(8) $\langle A_P \rangle$	(9) $B_{max}(\delta)$
7 Iris	S	200* 10	**260**	**220**	**155**	7.139	15 ± 5	+25 ± 15	1980	-69 ± 10	43100 ± 9300	360 ± 180
									1984	-21 ± 8	31900 ± 7700	940 * 150
									1991	-56 ± 10	40900 ± 9100	2010 ± 620
9 Metis	S	—	215	170	135	5.078	O*5	+20 * 10	1984	+61 ± 10	27000 ± 5800	570 * 200
							180 ± 5	+30 ± 10		−69 ± 11	2760016000	420 ± 220
									1986	-20 ± 7	21500 ± 5400	1100 ± 170
										+20 ± 7	21500 ± 5400	1100 ± 170
12 Victoria	s	113 ± 3	–	—	—	8.662	242 ± 3	+17 *4	1982	-30 ± 5	10000 ± 2000	290-400
									1989	−2 ± 4	10000 ± 2000	350-440
216 Kleopatra	M	135 ± 2	250	90	70	5.385	71*3	+19 ± 3	1985	−58 ± 4	15900 * 3500	680 * 130
654 Zelinda	c	127 ± 4	–	—	–	31.9	—	–	1988	–	12700 ± 2500	<140

Table II — notes by column:

(1) Taxonomic classification (Tholen 1989) based on visual and infrared data.

(2) Tedesco and Veeder (1992). These "radiometric diameters"' (in km) assume a spherical asteroid that obeys the Standard Thermal Model (Lebofsky and Spencer 1989). Departures from sphericity may bias these estimates to an extent that depends on the asteroid's shape and its orientation at the time of the IRAS observation (Brown 1985) .

(3) Adopted axis dimensions (in km) based on a combination of radiometric, lightcurve, and occultation data (see text). We adopt an uncertainty of 15'% in each dimension.

(4) Except for Victoria (Erikson 1990). synodic periods (in days) are from Lagerkvist *et al. (* 1989) and references therein. See also Lagerkvist *et al.* (1987, 1988).

(5) Ecliptic coordinates (in degrees) of the spin vector. Except for Victoria (Tempesti and Burchi 1%9), all pole directions are those of Magnusson (1986, 1990). Alternative pole directions, which may differ slightly from those listed, are noted in the text.

(6) Year of radar observation. All observations were performed with the 12.6-cm Arecibo radar. except for the 1991 Iris observations (de Pater et *al.* 1994), which were performed with the 3.5-cm Goldstone radar.

(7) Sub-radar latitude over the duration of observation corresponding to the listed pole direction and its uncertainties.

(8) Unweighted average projected area (in km^2) of the model ellipsoid over all rotation phases for the duration of observation. The uncertainty in the model's projected area incorporates the uncertainties in the axis dimensions and pole direction.

(9) Maximum edge-to-edge bandwidth (in Hz) over the duration of observation for the *a priori* ellipsoid with the listed pole direction and synodic spin period and all associated uncertainties. Since there are no *a priori* ellipsoids for Victoria and Zelinda, we assume the maximum breadth sampled is between 1.0 and 1.2 times the IRAS diameter.

Table III : Radar Properties by Experiment

Target	Year	(1) OC SNR	(2) B_{EQ} (Hz)	(3) B_{HP}/B_{ZC}	(4) σ_{OC} (km²)	(5) μ_C	(6) $\hat{\sigma}_{OC}$
Iris (A)	1980	22	277	0.70	5\$00 (1500)	0.08 (0.03)	0.14 (0.05)
	1984	28	643	0.54	2900 (700)	0.19 (0.03)	0.09 (0.03)
Iris (G)	1991	19	1476	0.55	4100 (1OOO)	0.19 (0.05)	0.10 (0.03)
Metis	1984	12	180	0.86	3500 (920)	0.18 (0.08)	0.13 (0.04)
	1986	13	640	0.61	2900 (730)	0.13 (0.05)	0.13 (0.05)
Victoria	1982	33	180	0.56	2100 (520)	0.14 (0.03)	0.21 (0.07)
	1989	54	160	0.60	2500 (620)	0.13 (0.05)	0.25 (0.08)
Kleopatra	1985	19	570	0.69	7100 (1800)	0.00 (0.05)	0.44 (0.15)
Zelinda	1988	37	80	0.56	2300 (580)	0.13 (0.03)	0.18 (0.06)

Table III — notes by column:

(1) The OC SNR is the signal-to-noise ratio for an optimally filtered, weighted sum of all spectra from an experiment.

(2) By definition (Tiuri 1964), $B_{EQ} = \Delta f\,[(\Sigma S_i)^2/\Sigma S_i^2]$, where S_i are the spectral elements, and Δf is the "raw" frequency resolution.

(3) B_{HP} and B_{ZC} are the half-power and zero-crossing bandwidths, respectively, of the weighted sum of all spectra from an experiment smoothed to a frequency resolution of $B_{EQ}/10$.

(4) σ_{OC} is the OC radar cross section. Assigned uncertainties are the root sum square of systematic calibration errors, estimated as 25% of the cross section values. and the standard deviation of the receiver noise in the equivalent bandwidth (B_{EQ}).

(5) μ_C is the circular polarization ratio (of SC to OC echo power). The standard deviations quoted for μ_C propagate from the receiver noise alone.

(6) The radar albedo, $\hat{\sigma}_{OC}$, is obtained by dividing σ_{OC} by the average projected area of the *a* priori model ellipsoid at the epoch of our observations, if available, or the projected area of a sphere with the IRAS diameter (see Table II). Uncertaintes propagate from those given for σ_{OC} and $\langle A_P \rangle$.

Table IV : Average radar properties

Target	Class	$\langle \mu_C \rangle$	$\langle \hat{\sigma}_{OC} \rangle$
Iris	S	0.14 (0.06)	0.10 (0.03)
Metis	S	0.14 (0.04)	0.13 (0.03)
Victoria	s	0.14 (0.03)	0.23 (0.05)
Kleopatra	M	0.00 (0.05)	0.44 (0.15)
Zelinda	C	0.13 (0.03)	0.18 (0.06)

Table IV: Weighted averages of μ_C and $\hat{\sigma}_{OC}$ from all Arecibo radar experiments for each target. For Iris, the uncertainty for $\langle \mu_C \rangle$ may encompass real variations in μ_C as a function of sub-radar latitude (see text).

Table V : Asteroid-meteorite associations

Mineralogy	Possible meteorite analogs	Meteorite properties: Bulk density (g cm^{-3})	Meteorite properties: Percentage abundance of metallics (wt)	Meteorite properties: Percentage abundance of metallics (vol)
M asteroids				
Metal	Irons	7.6	97	97
Metal + enstatite	Enstatite chondrites	3.6	32	19
S asteroids				
Metal + olivine + pyroxene	Stony irons	4.9	50	30
Metal + olivine + pyroxene	Ordinary chondrites			
	H	3.6	24	12
	L	3.5	14	8
	LL	3.5	2	1
C asteroids				
Hydrated silicates + carbon-organics-opaques	Carbonaceous chondrites (CI 1 and CM2)	2.6	11	6

Table V: From Ostro *et al.* (1991). Meteorite analogs are from Lipschutz *et al. (1989).* Typical densities and approximate abundances of metallics (native metals and metal sulfides) are from Tables 2.1 and 4.1 of Dodd (1981). Table 24 of Buchwald (1975), Table 2 of Keil (1%8), and Table 4.6 of Glass (1982). High-iron (H) and low-iron (L) chondrites are an order of magnitude more abundant than very low iron (LL) and enstatite (E) chondrites. The extremely rare Q asteroids might be analogous to ordinary chondrites (McFadden *et* al. 1989).

Table VI : Future Radar Opportunities

Target	(1) Current Total SNR	(2) Future SNR per day	(3) Year
Iris	28	100	2000
		480	2006
Metis	13	140	1997
Victoria	54	220	2007
Kleopatra	19	330	1999
Zelinda	37	1150	2002
		1080	2007

Table VI — notes by column:

(1) The OC SNR from the best experiment to date (see Table III).

(2) Predicted OC SNR per day for nominal parameters of the upgraded Arecibo radar. For each prediction we assume an equatorial view and a radar cross section given by the product of the target's radar albedo (Table IV) and the projected area of a sphere with the target's radiometric diameter (except for Metis where we have assumed a diameter of 170 km). We believe these predictions to be reliable within -30%.

(3) Selected opportunities between 1997 and 2007. The Arecibo upgrade is expected to be complete by mid-1996.

FIGURE CAPTIONS

Figure 1: Arecibo radar spectra of Iris obtained in 1980 (top panel) and 1984 (bottom panel). Echo power. in standard deviations of the noise, is plotted versus Doppler frequency relative to that of hypothetical echoes from the asteroid's center of mass. The solid and dotted lines plot the OC and SC echoes, respectively, smoothed to a frequency resolution of 30 Hz. Each spectrum is a weighted sum of independent spectra obtained at different asteroid rotation phases, which are depicted in the inset with a radial "error bar" proportional to the standard deviation of each spectrum included in the average. The arrow indicates zero phase. as defined in Table 1, and phase increases in the counter-clockwise sense. There is no correspondence bet ween 1980 and 1984 phases. The vertical extent of the shaded boxes shows *1 standard deviation of the noise, while the horizontal extent shows the expected range for the edge-to-edge bandwidth (B_{max}) based on radiometric and lightcurve constraints on the asteroid's size, shape, and spin vector (see Table II).

Figure 2: Goldstone 3.5-cm radar spectrum of Iris obtained in 1991, smoothed to a frequency resolution of 240 Hz. (See caption to Fig. 1.)

Figure 3: OC spectra of Iris from individual runs in 1980, each smoothed to a frequency resolution of 30 Hz. (Spectrum 4 is the weighted sum of two runs.) The frequency scale below spectrum 1 applies to all spectra. The vertical bar at the origin indicates ± 1 standard deviation of the noise. (See also caption to Fig, 1).

Figure 4: Weighted sums of OC echo spectra of Iris from 1984 within the rotation phase intervals depicted in the polar plot, each smoothed to a frequency resolution of 30 Hz.. The frequency scale below spectrum 5 applies to all spectra. The vertical bar at the origin indicates ±1 standard deviation of the noise. (See also caption to Fig. 1).

Figure 5: OC spectra of Iris obtained in 1984 within *narrow* rotation phase ranges (cf. Fig. 4). A radar spike appears in spectrum "b" centered at a Doppler frequency of -305 Hz, but not in adjacent rotation phase ranges (a and c). The spectra are smoothed to a frequency resolution of 90 Hz to maximize the spike's height, The shaded boxes are as in the lower panel of Fig. 1.

Figure 6: Arecibo radar spectra of Metis obtained in 1984 (top panel) and 1986 (bottom panel). The solid and dotted lines plot the OC and SC echoes, respectively, smoothed to frequency resolutions of 50 Hz (top) and 150 Hz (bottom). The notation is the same as in Fig, 1. Various lightcurve-based pole solutions (see text) result in different predictions for the edge-to-edge bandwidth in 1984 (stacked shaded boxes), but identical predictions in 1986. The innermost zero crossings of the 1984 spectrum seem to favor the D 1, D2, and M2 pole solutions (see text).

Figure 7: Weighted sums of OC echo spectra of Metis from 1984 within the rotation phase intervals depicted in the polar plot, each smoothed to a frequency resolution of 60 Hz. The frequency scale below spectrum 6 applies to all spectra.

Figure 8: Weighted sums of OC echo spectra of Metis from 1986 within the rotation phase intervals depicted in the polar plot, each smoothed to a frequency resolution of 100 Hz. The frequency scale below spectrum 2 applies to all spectra.

Figure 9: OC spectra of Metis obtained in 1984 within narrow rotation phase intervals (cf. Fig. 7). A radar spike appears in spectra" a" and "b" centered at a Doppler frequency of −85 Hz. The spectra are smoothed to a frequency resolution of 50 Hz in order to maximize the spike's height. No statistically significant feature is present in spectrum "c," which has a higher noise level than the other two spectra. The shaded boxes show edge-to-edge bandwidth predictions based on the D 1 and D2 pole solutions (see Fig. 6).

Figure 10: Radar Doppler spectra of Zelinda obtained at Arecibo in 1988. (a): Weighted average OC spectra from each run (four 4-minute accumulations) smoothed to a frequency resolution of 12 Hz. The weighted average rotation phase is indicated above each plot. (b): Weighted average OC spectra for each day at the raw 4-Hz frequency resolution. (c): Weighted average OC and SC spectra for the entire experiment at the raw 4-Hz frequency resolution. The horizontal extent of the shaded boxes is derived from fitting the spectrum with an $S(f)$ model (Eq. 3) for $1 < n \leq 6$. The best-fit value of n is 2.4 ± 0.7 (arrows labeled "L. S,"). The arrows labeled "IRAS" show the maximum edge-to-edge bandwidth corresponding to the IRAS diameter and an equatorial view.

Figure 11: OC spectra of Zelinda from individual 4-minute accumulations obtained at Arecibo on 18 January 1988 (cf. Fig. 10). The rotation phase is indicated above each spectrum. All spectra are smoothed to a frequency resolution of 12 Hz, and the frequency scale below the last spectrum applies to all spectra. A radar spike appears at 92.4° and disappears abruptly at 99°.

Figure 12: Weighted sums of OC echo spectra of Kleopatra from 1985 within the rotation phase intervals depicted in the polar plot, each smoothed to a frequency resolution of 60 Hz. The frequency scale below spectrum 4 applies to all spectra. The shaded boxes show interval estimates of the spectral edge positions based on the *a priori* ellipsoid model (see text).

Figure 13: Arecibo radar spectra of Kleopatra obtained in 1985. The panels represent averages over different ranges of asteroid rotation phase, as indicated by the insets (cf. Fig. 1). The solid and dotted lines plot the OC and SC echoes, respectively, which are smoothed to a frequency resolution of 60 Hz. The shaded boxes show interval estimates of the spectral edge positions based on the *a priori* ellipsoid model (see text).

Figure 14: OC spectra of Kleopatra (thin lines) averaged within four rotation phase intervals as indicated by the phase plot. Phases are averaged modulo 180" to maximize the SNR. The radar signature of the best-fit biaxial ellipsoid, with a reduced chi square of 1.10, is shown by thick lines, and the difference (data - model) is shown by the dashed lines. The vertical bar at the origin of each spectrum shows ±1 standard deviation of the noise. and the shaded boxes are as in Fig. 12. Note that a deficit of echo power near zero Doppler frequency is present over a broad range of rotation phase (spectra 1-3).

Figure 15: Same as Fig. 14, except that the model is composed of two biaxial ellipsoids in contact, with a reduced chi square of 0.98 (see text).

Figure 16: Adapted from Dunham (1992). Chords from the 1991 Kleopatra occultation (solid lines). Dashed lines are non-detections, one of which is uncertain. The longest chord suggests a large topographic feature.

Figure 17: Arecibo radar spectra of Victoria obtained in 1982 (top panel) and 1989 (bottom panel) at the raw 1O-HZ frequency resolution. The shaded boxes correspond to the $S(f)$ fitting procedure (cf. Fig. 10 [cl) with $1 \leq n \leq 6$. The brackets show interval estimates of the spectral edges based on the pole direction of Tempesti and Burchi (1969) and assuming that the maximum breadth sampled was between 1.0 and 1.2 times the IRAS diameter (see Table II).

Figure 18: Comparison of radar and lightcurve constraints on Victoria's pole direction shown in a rectangular projection of geocentric ecliptic coordinates. The radar constraints are obtained by fitting each spectrum shown in Fig. 17 with a spherical model that has a diameter between 1.0 and 1.2 times the IRAS diameter (Table II) and a cosine scattering law exponent between 1 and 6. The aspect angle ($a = \delta + 90$") between the radar line of sight and the asteroid's spin vector is adjusted to maintain the best fit while the diameter and scattering law exponent are perturbed within the specified limits. This procedure yields an allowed range for α, which defines an annulus (dotted lines) centered on the asteroid's coordinates (plus symbol). The sense of rotation is not determined with this method, so there are actually two annuli for each date corresponding to $\pm\delta$. The intersections of the annuli (outlined in bold) define four possible regions for the pole coordinates that are consistent with both spectra. The pole direction derived by Tempesti and Burchi (1%9), shown by the filled circle with error bars. is incompatible with the radar constraints.

Figure 19 (a): Weighted sums of OC echo spectra of Victoria obtained in 1982 within four -50° rotation phase intervals, smoothed to a frequency resolution of 30 Hz. Individual runs (or in some cases two runs that nearly coincide in phase) are indicated by letters (a-c) within each group. The frequency scale below the group 1 spectrum is the same for all spectra. (b): Weighted sums of OC echo spectra within each of the phase sub-groups defined in (a). The weighted average phase (degrees) and phase sub-group are indicated, respectively, in the upper left and right of each spectrum.

Figure 20 (a): Weighted sums of OC echo spectra of Victoria obtained in 1989 within three -50° rotation phase intervals, smoothed to a frequency resolution of 30 Hz. Individual runs are indicated by letters (a-c) within each group. These are intended to coresond roughly to the group designations in Fig, 19. The frequency scale below the group 3 spectrum is the same for all spectra. (b): Weighted sums of OC echo spectra within each of the phase sub-groups defined in (a). The weighted average phase (degrees) and phase sub-group are indicated, respectively, in the upper left and right of each spectrum.

Figure 21 (a): Asteroid radar albedo versus diameter for selected MBAs. Each of our targets is identified by a three-letter abbreviation, and all others by a symbol indicating taxonomic class. The radar albedos of MBA targets not discussed in this paper are *taken* from Table 2 of Ostro *et al. (1991).* (b): Reflection coefficient (R) for meteorite types (Table V). The curves show R as a function of porosity based on the average of three empirically determined functions (OCS85, Garvin *et* al. 198S, Ulaby *et al.* 1990) over the range of lunar soil porosities. These curves are probably accurate to& 25%. The oval fields show ranges of R expected for several meteorite types on the basis of laboratory investigations (Kelley *et al.* 1953, Nielsen 1974, Pettengill et *al.* 1988) of "loaded dielectries." Cross-hatched fields show measurements of R for six meteorite specimens (Campbell and Ulrichs 1969).

Figure 1

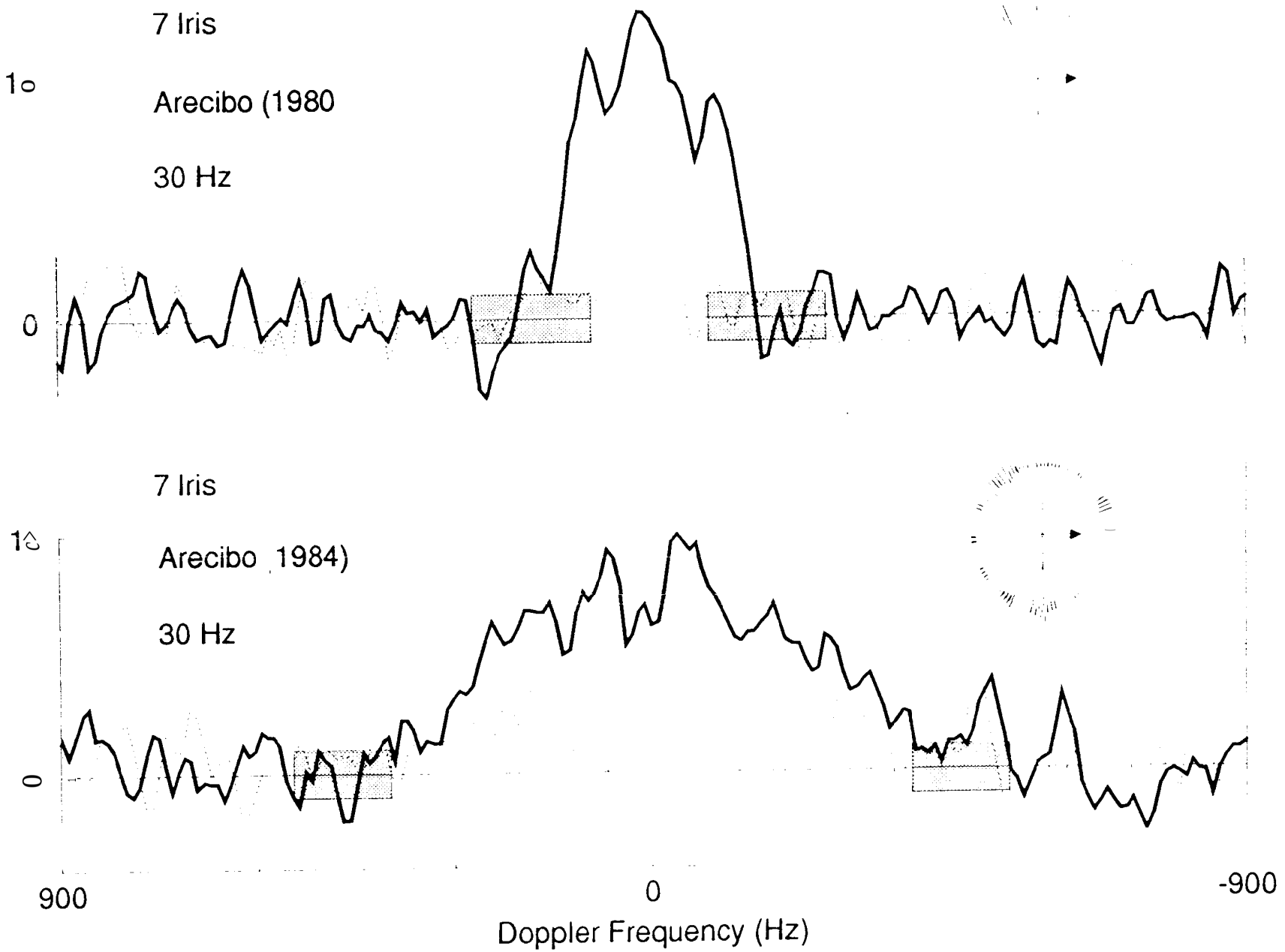
7 Iris
Arecibo (1980
30 Hz
7 Iris
Arecibo 1984)
30 Hz
0
900
0
-900
Doppler Frequency (Hz)

Figure 2

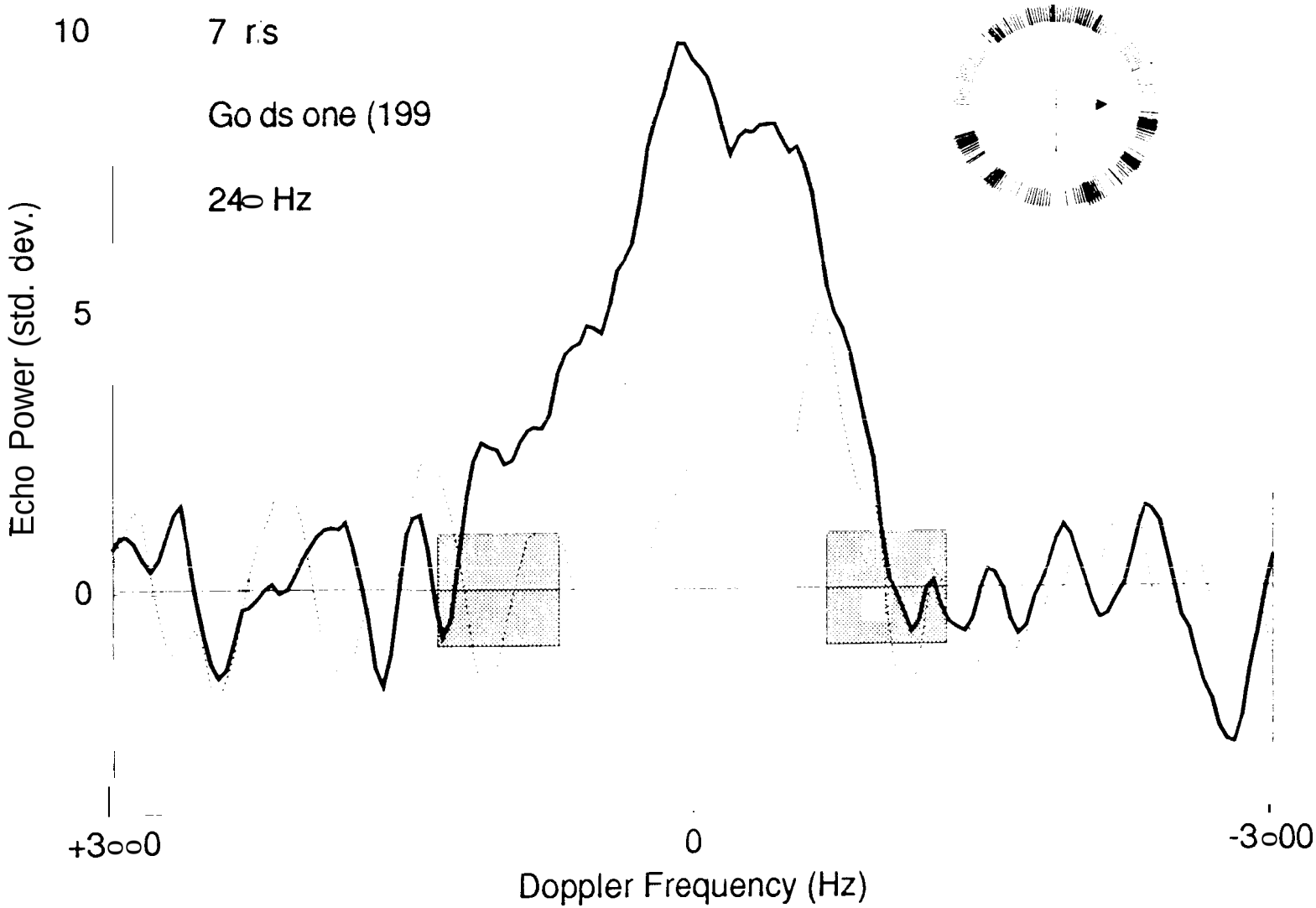
10
7 r.s
Go ds one (199
24o Hz
Echo Power (std. dev.)
5
0
+3oo0
0
-3o00
Doppler Frequency (Hz)

Figure 3

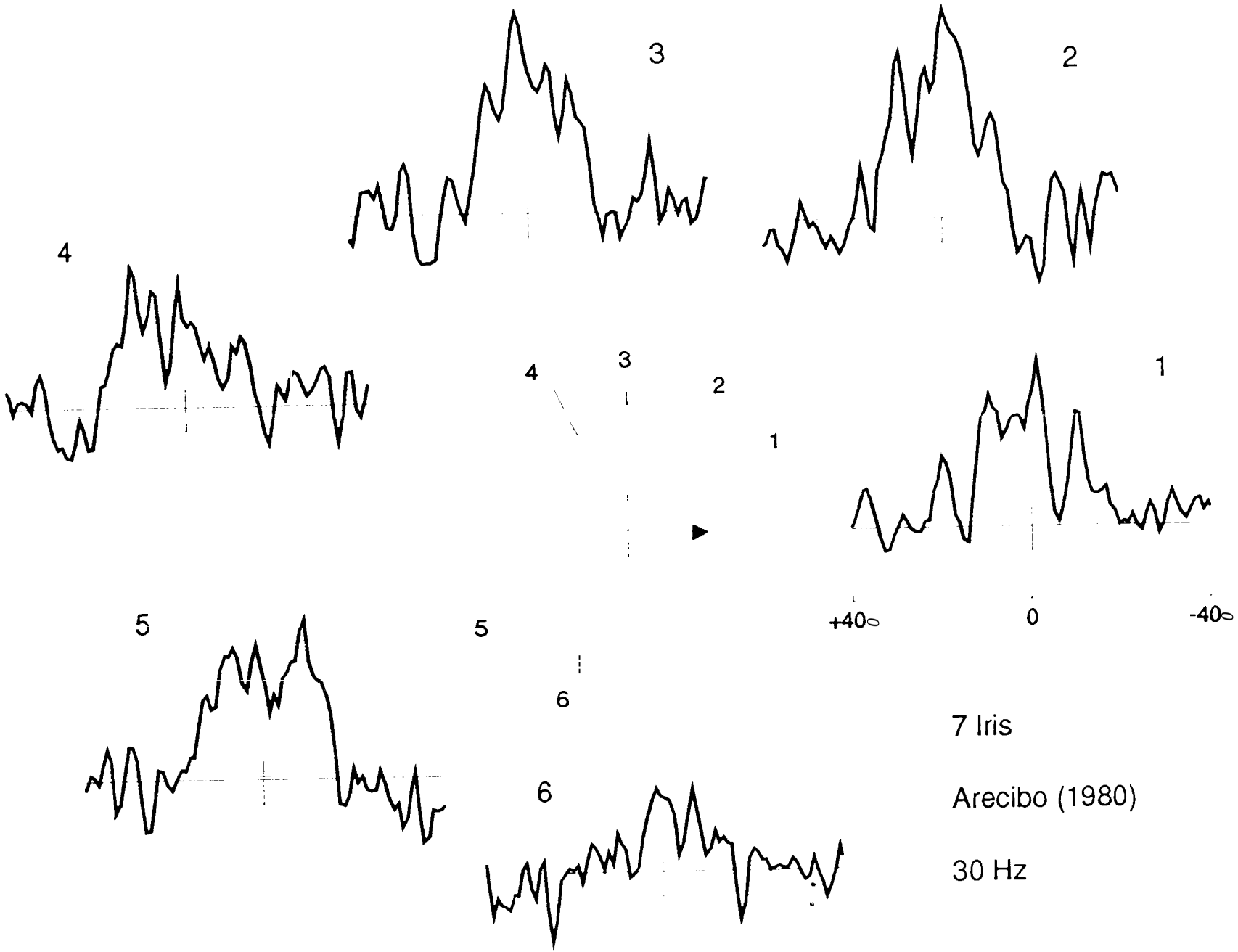

Figure 4

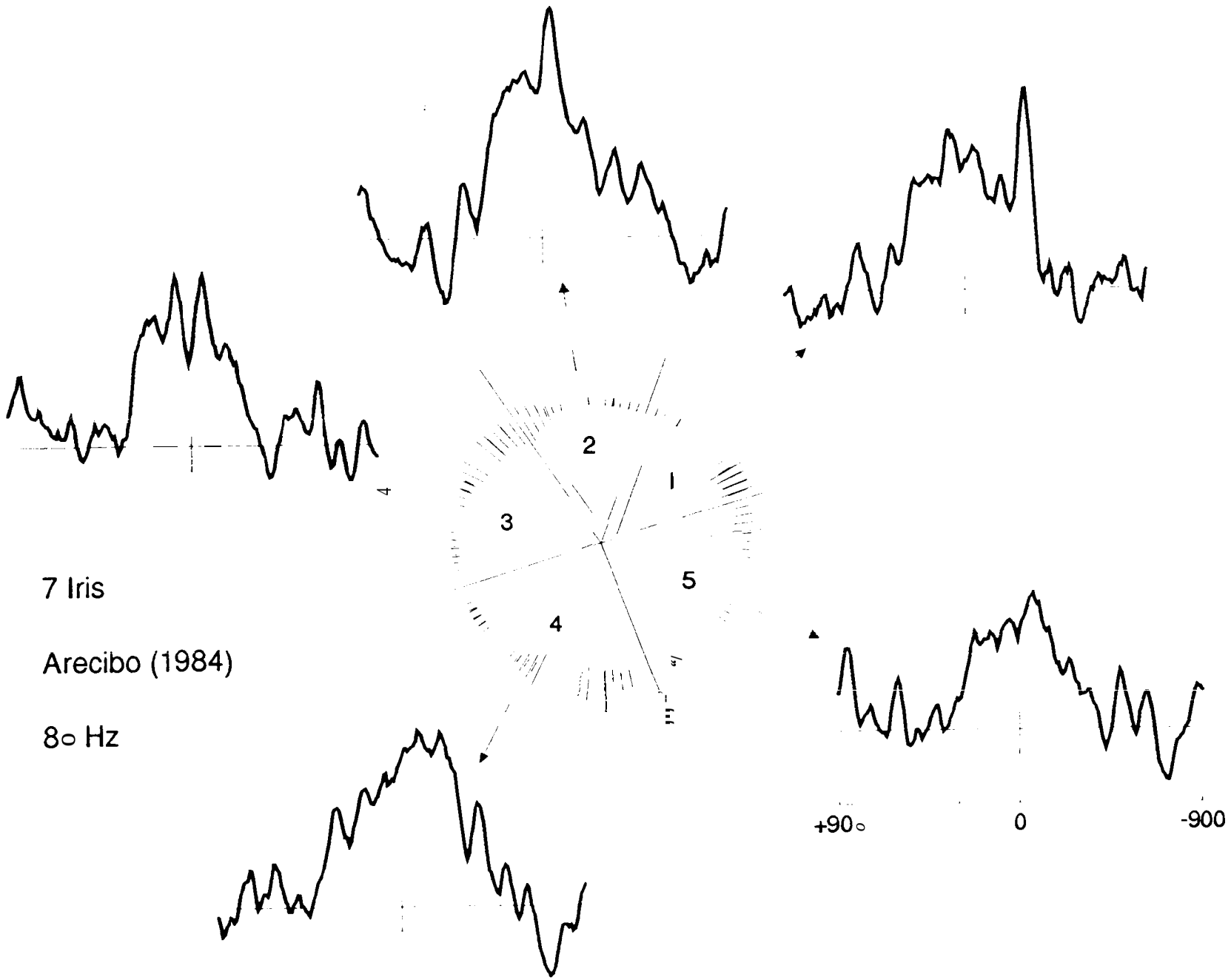

7 Iris

Arecibo (1984)

8∘ Hz

Figure 5

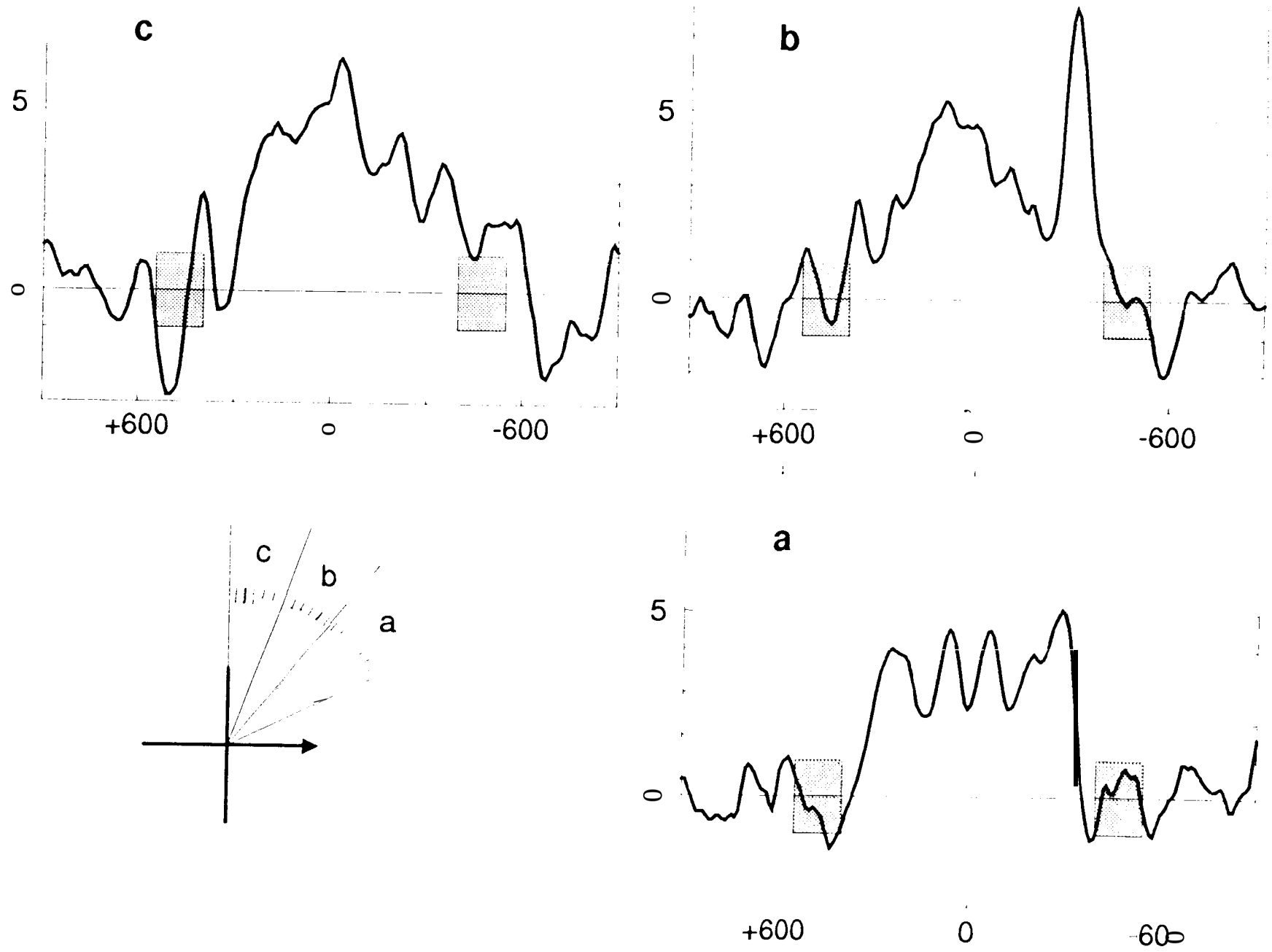

Figure 6

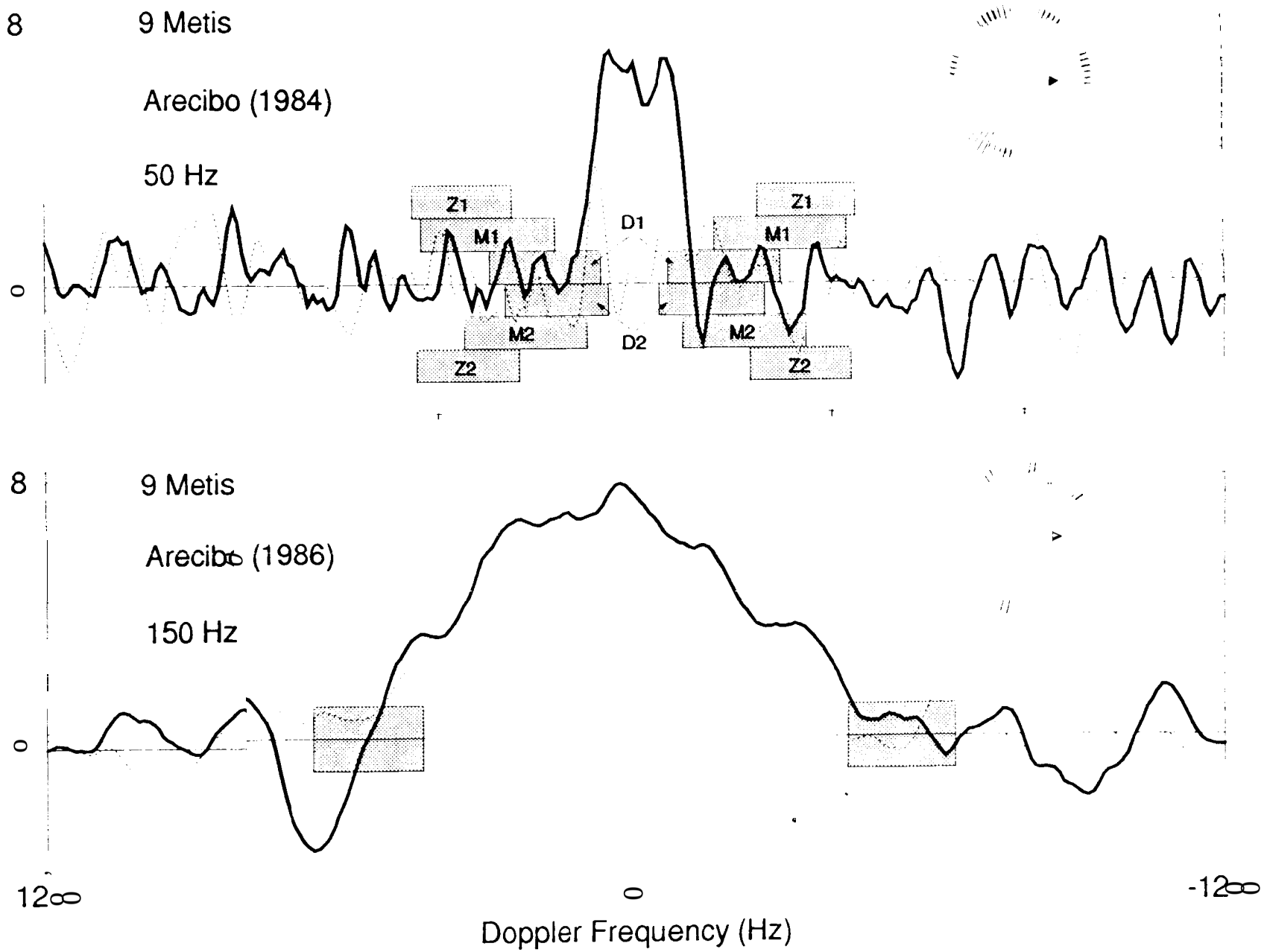
8
9 Metis
Arecibo (1984)
50 Hz
Z1
M1
M2
Z2
D1
D2
Z1
M1
M2
Z2
0
8
9 Metis
Arecibo (1986)
150 Hz
0
12∞
0
-12∞
Doppler Frequency (Hz)

Figure 7

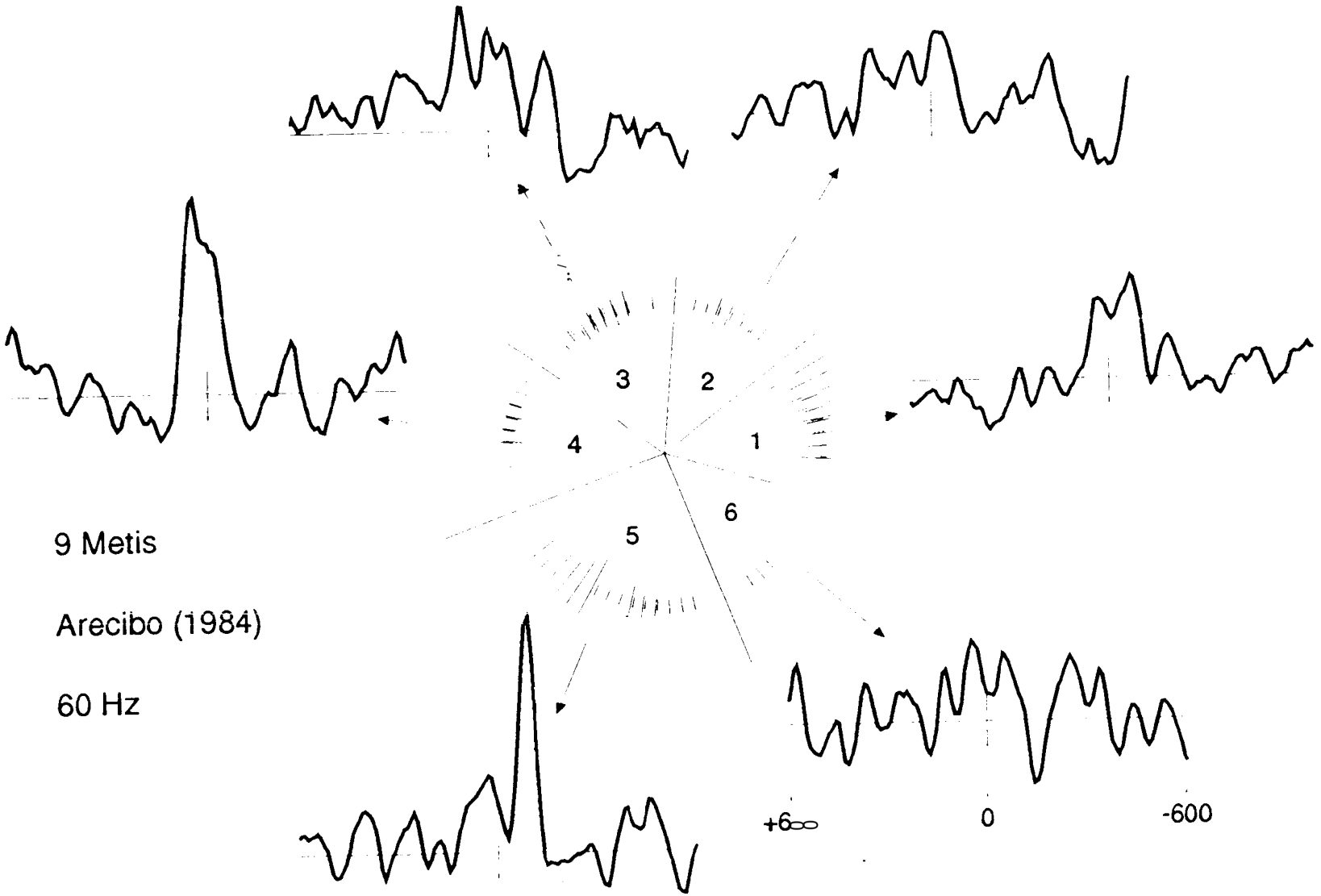

Figure 8

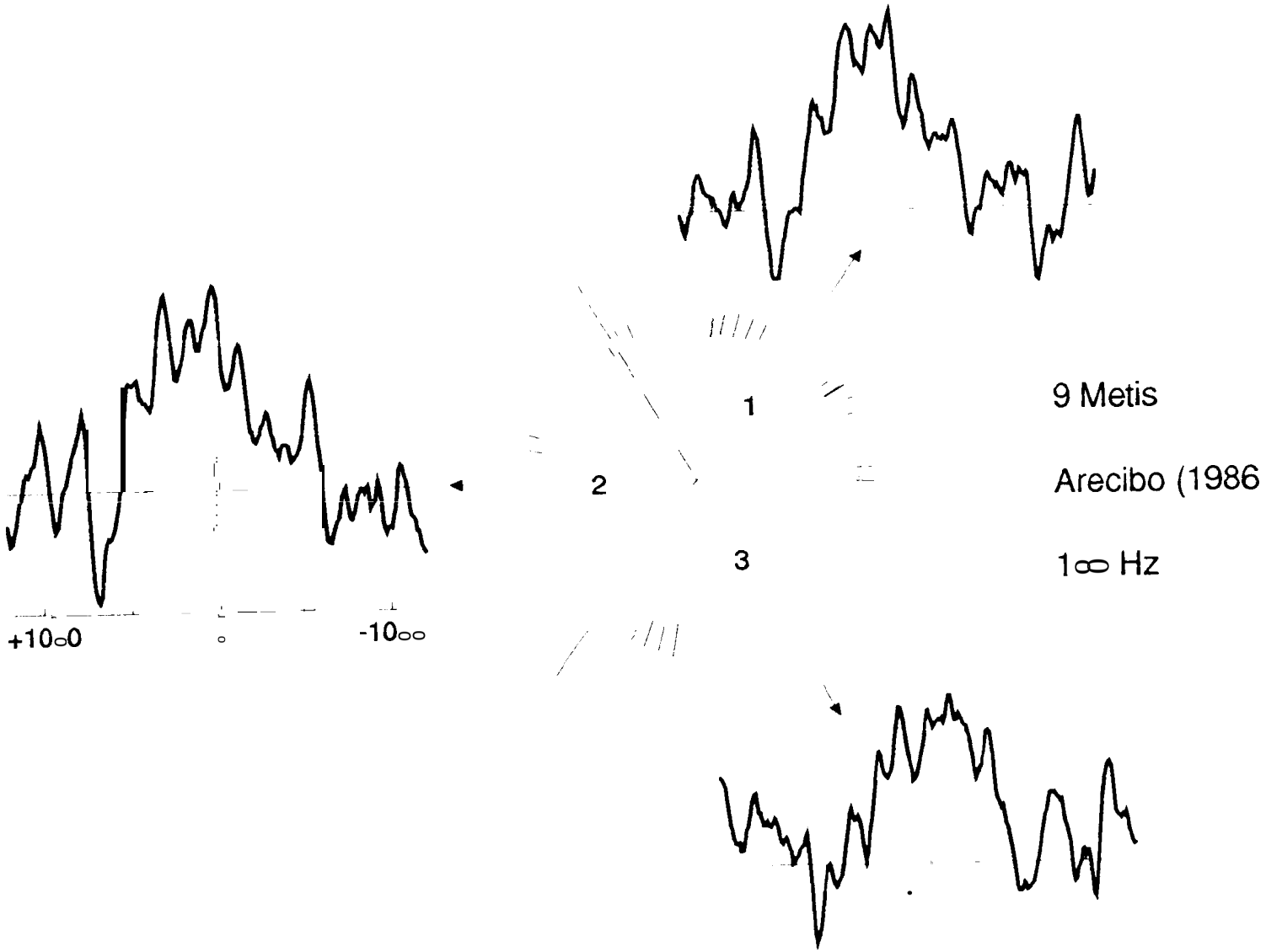

Figure 9

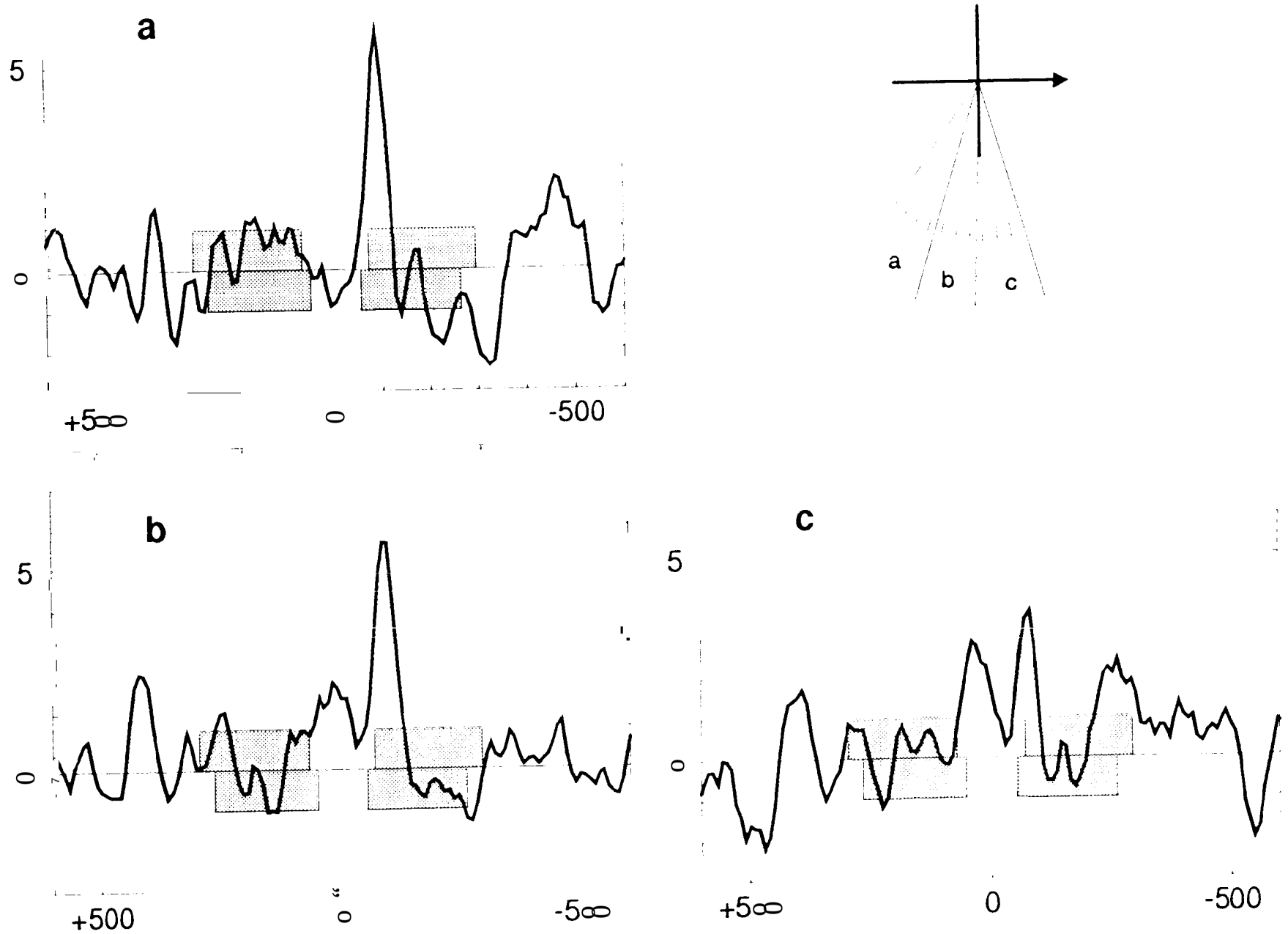

Figure 10 (a)

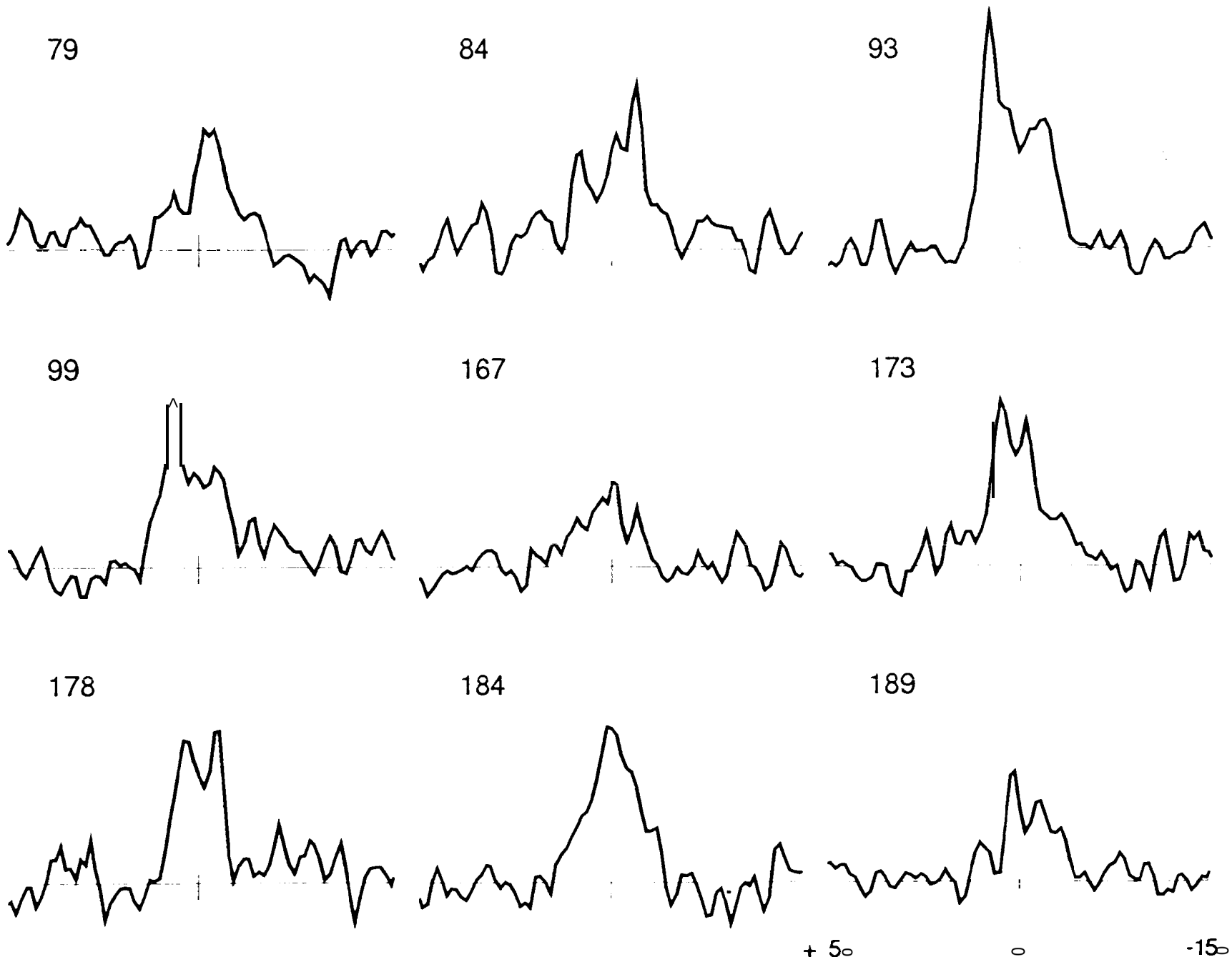

Figure 10 (b)

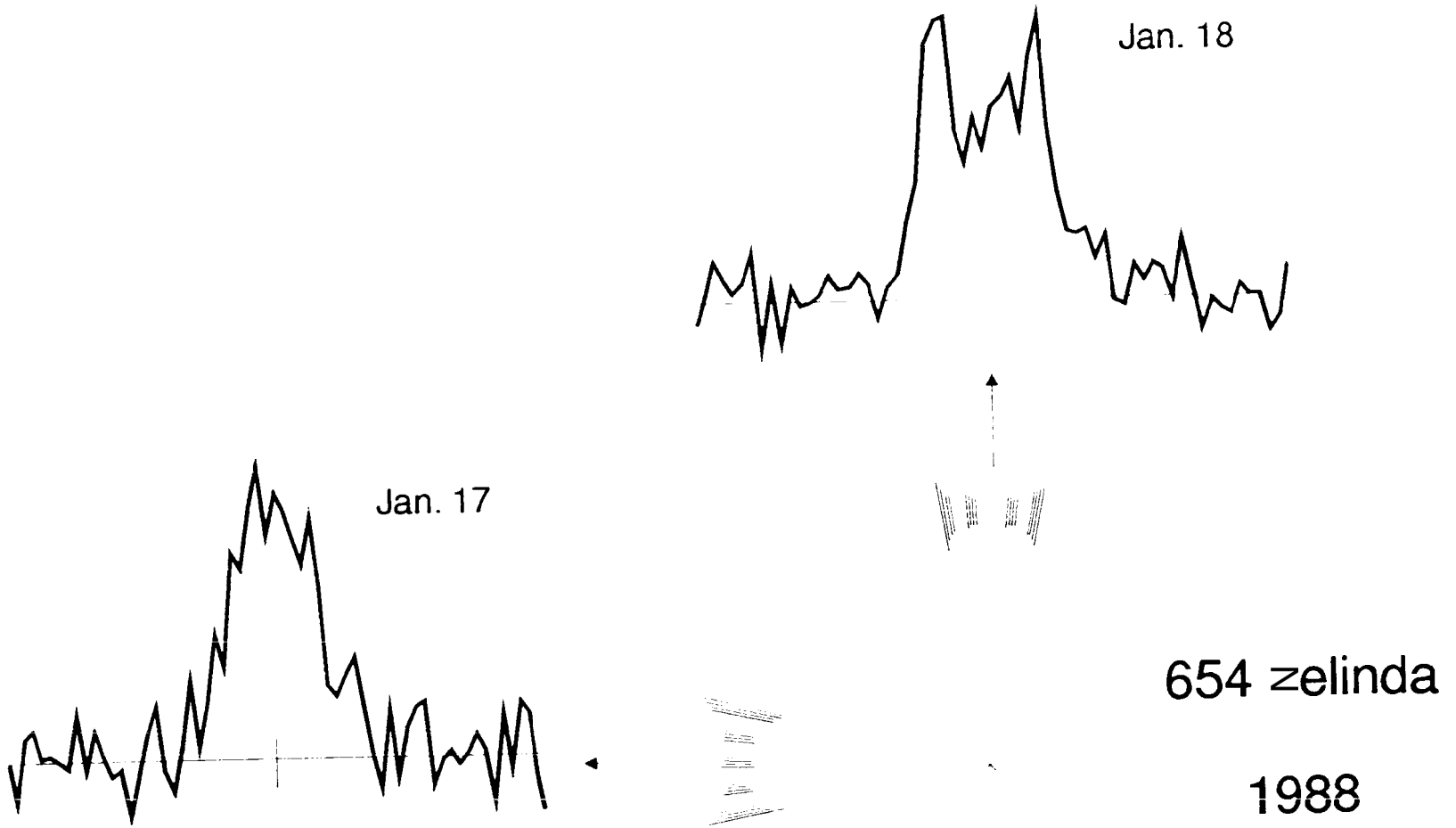

654 Zelinda

1988

4 Hz

Figure 10 (c)

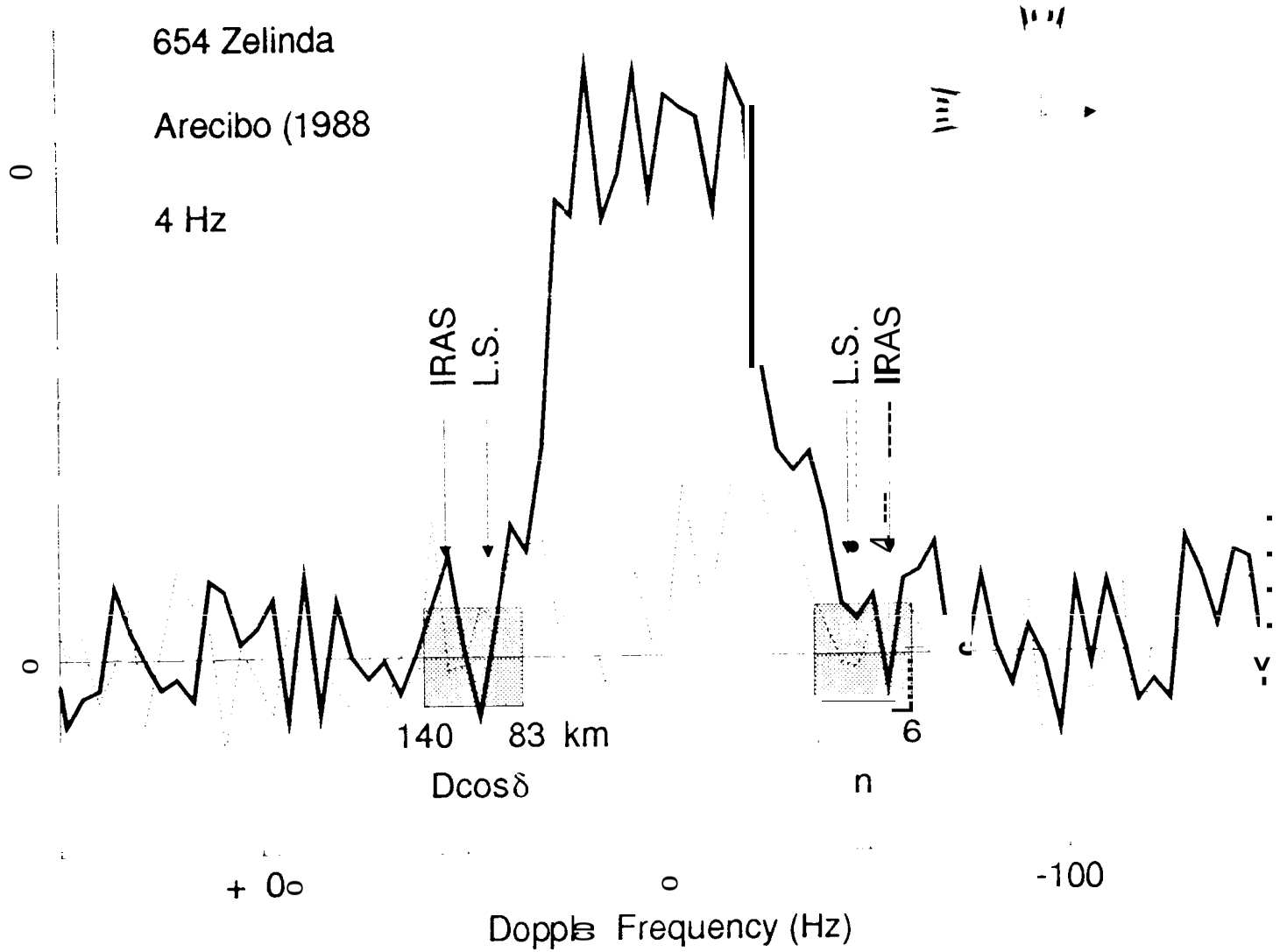
654 Zelinda
Arecibo (1988
4 Hz
IRAS
L.S.
L.S.
IRAS
140
83 km
6
Dcosδ
+ 0o
o
-100
Doppler Frequency (Hz)

Figure 11

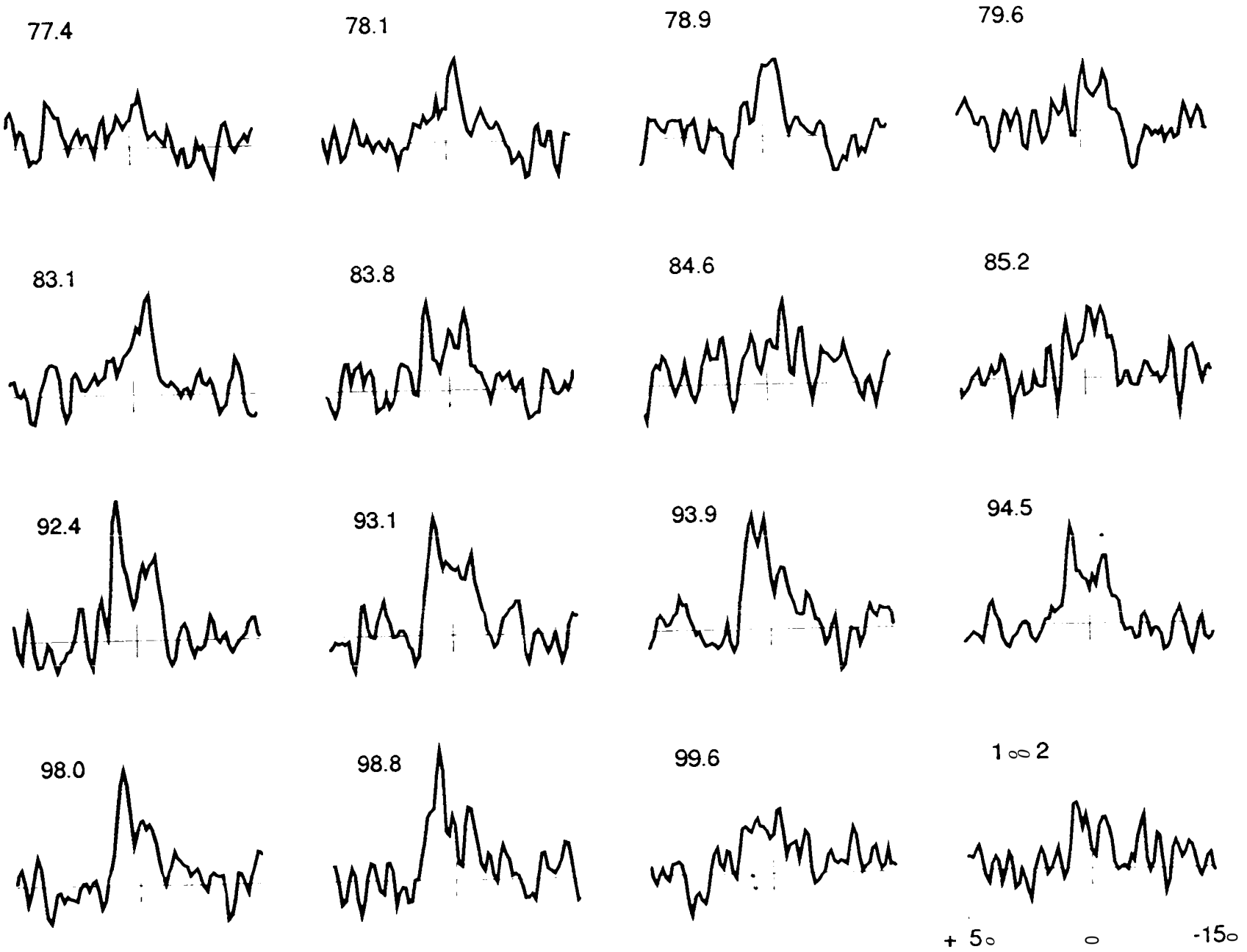
77.4
78.1
78.9
79.6
83.1
83.8
84.6
85.2
92.4
93.1
93.9
94.5
98.0
98.8
99.6
1 ∞ 2
+ 5∘
0
-15∘

Figure 12

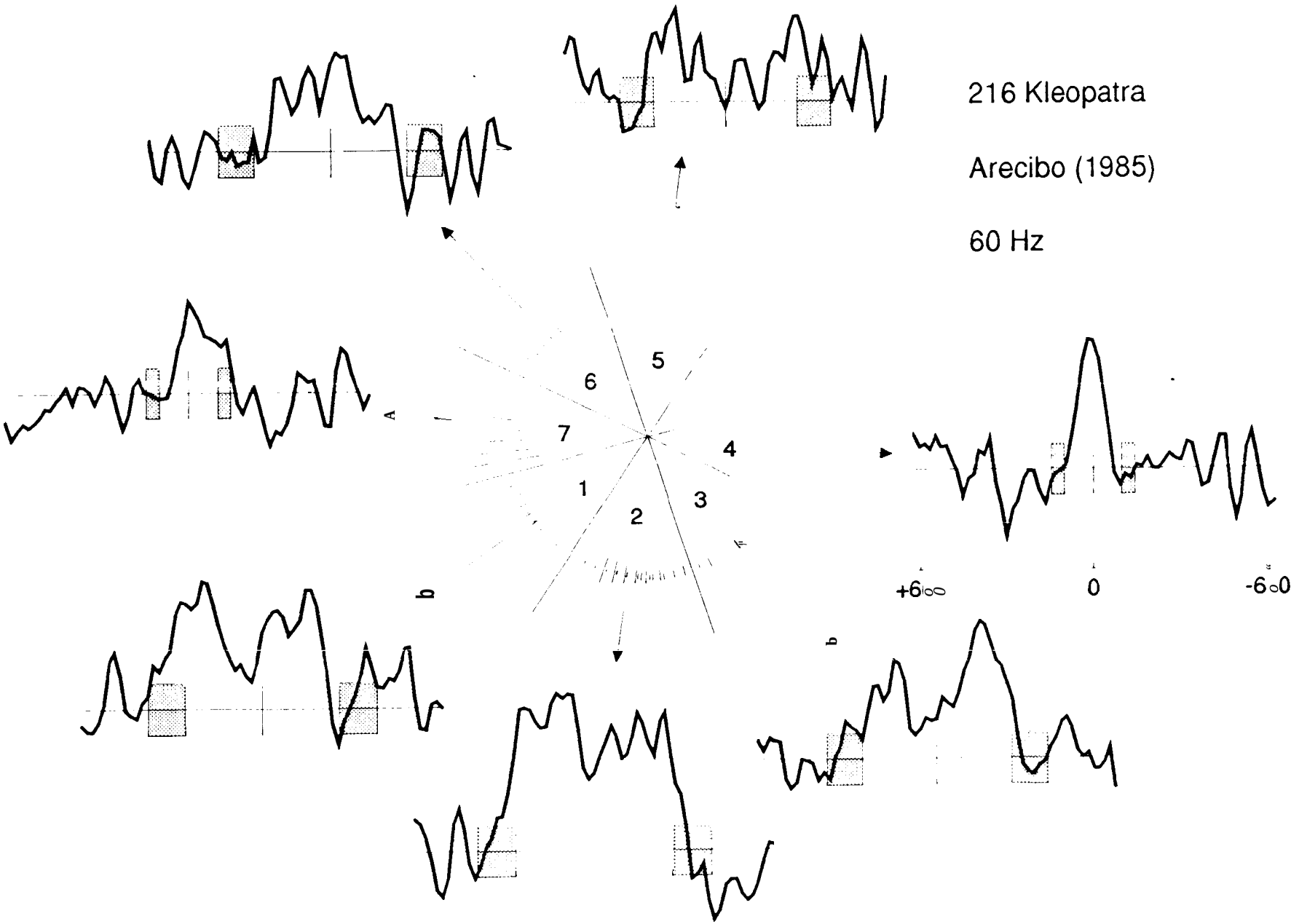

Figure 13

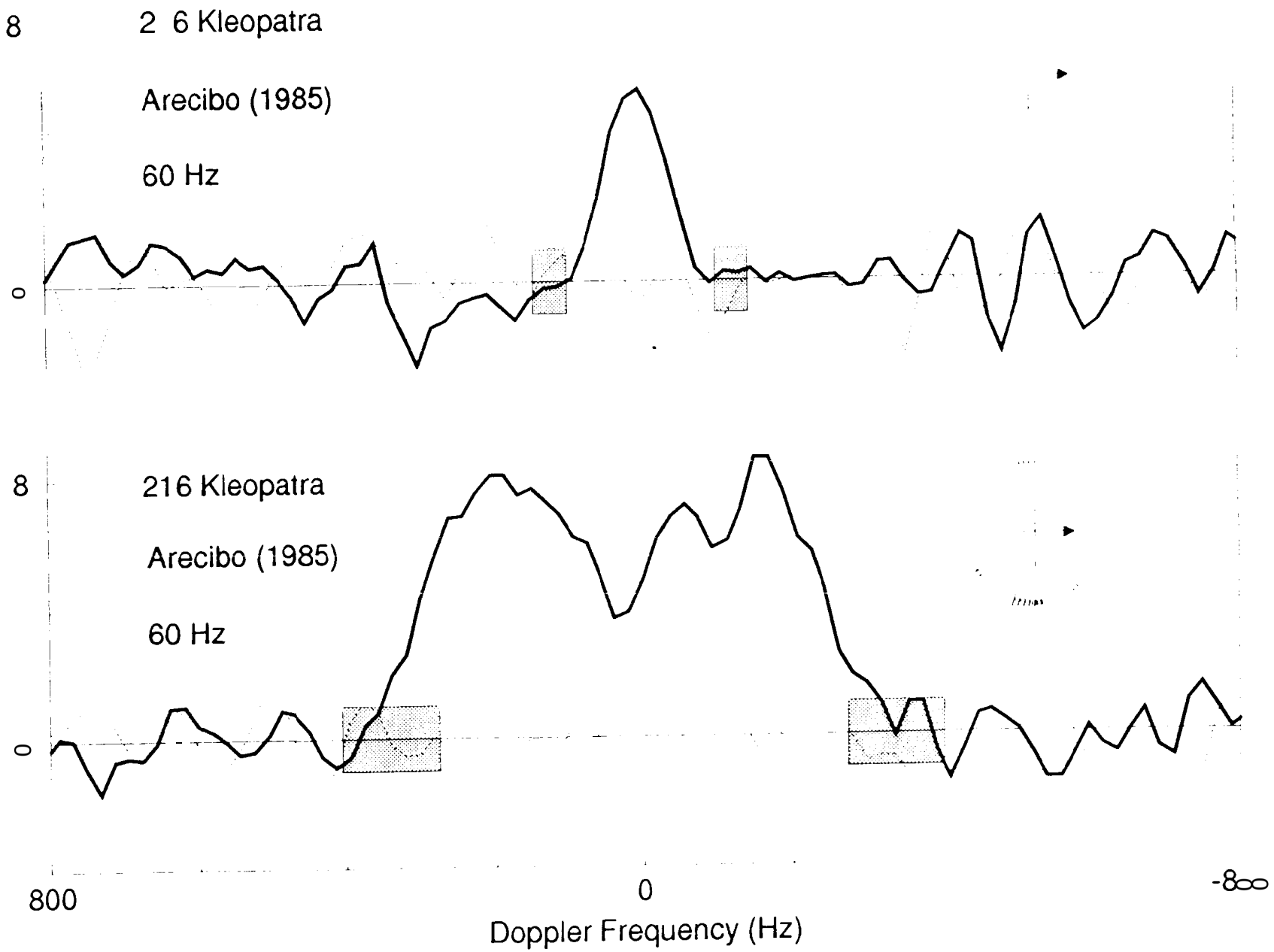
8
2 6 Kleopatra
Arecibo (1985)
60 Hz
0
8
216 Kleopatra
Arecibo (1985)
60 Hz
0
800
0
-800
Doppler Frequency (Hz)

Figure 14

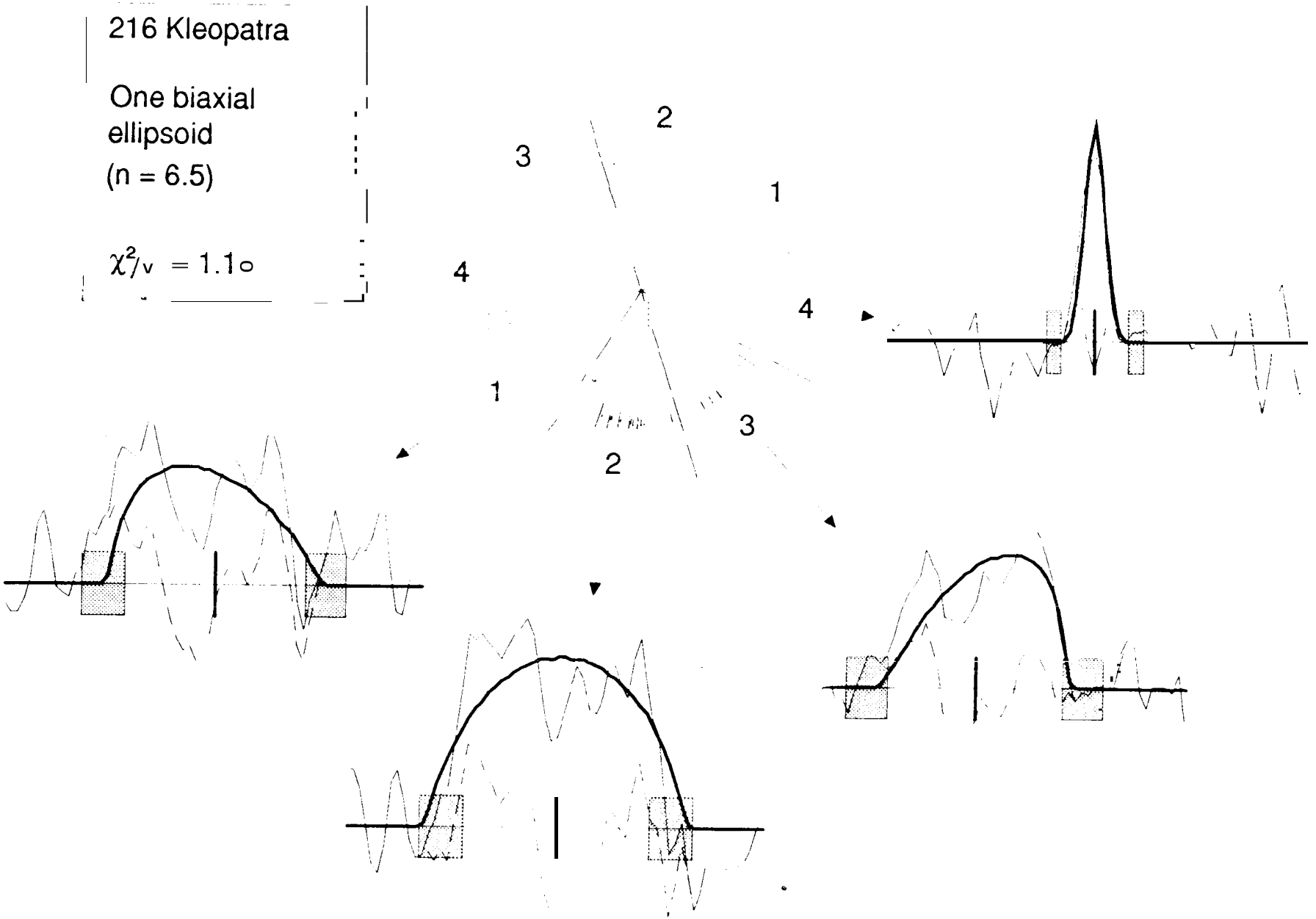

Figure 15

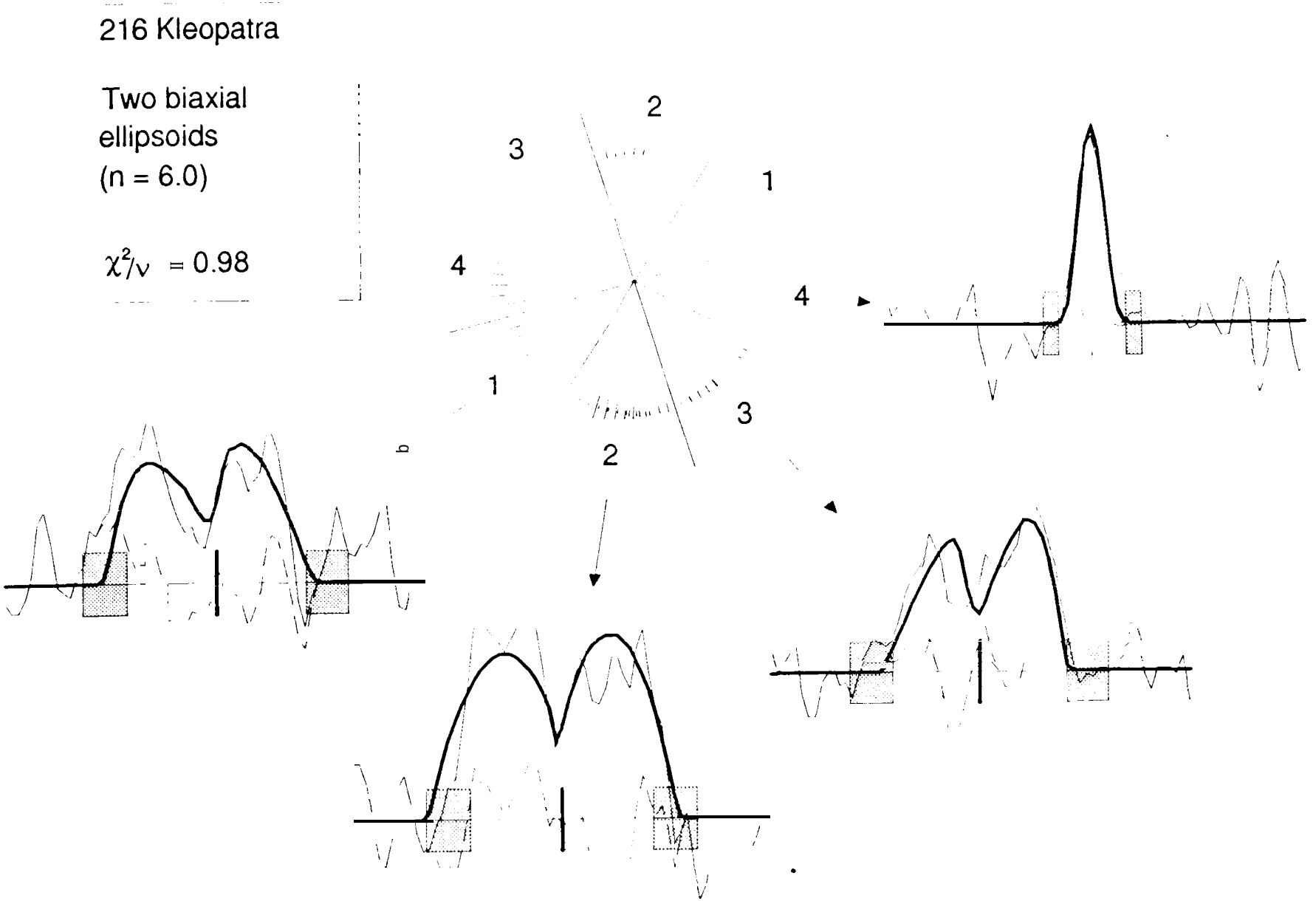
216 Kleopatra
Two biaxial ellipsoids (n = 6.0)
χ^2/ν = 0.98
1
2
3
4
1
2
3
4

Figure 16

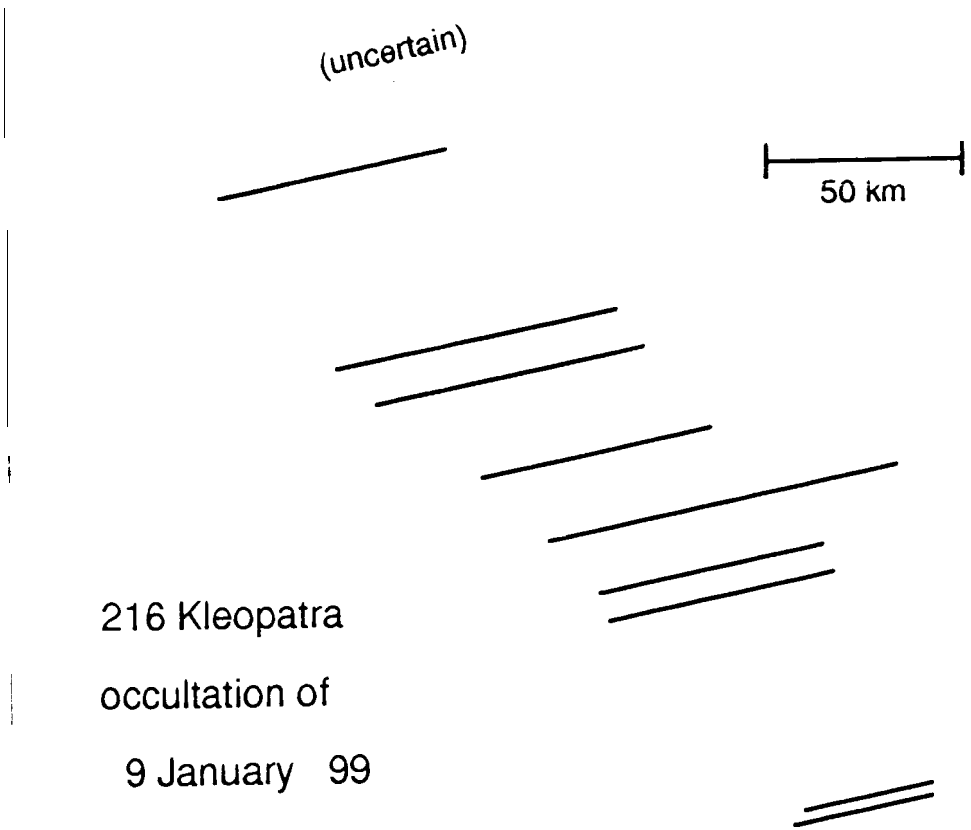

Figure 17

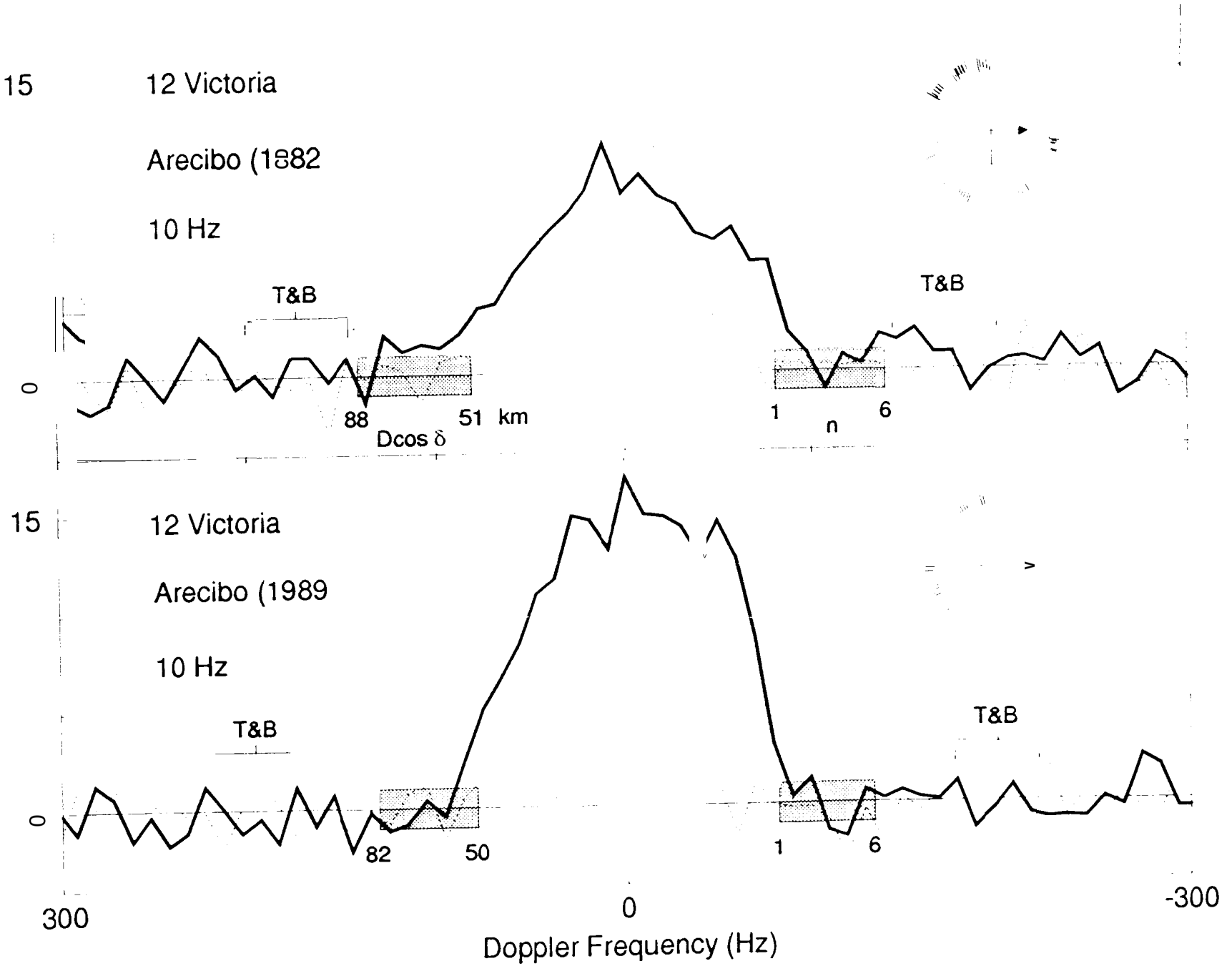
15
12 Victoria
Arecibo (1982
10 Hz
T&B
T&B
0
88
51 km
Dcos δ
1
6
n
15
12 Victoria
Arecibo (1989
10 Hz
T&B
T&B
0
82
50
1
6
300
0
-300
Doppler Frequency (Hz)

Figure 18

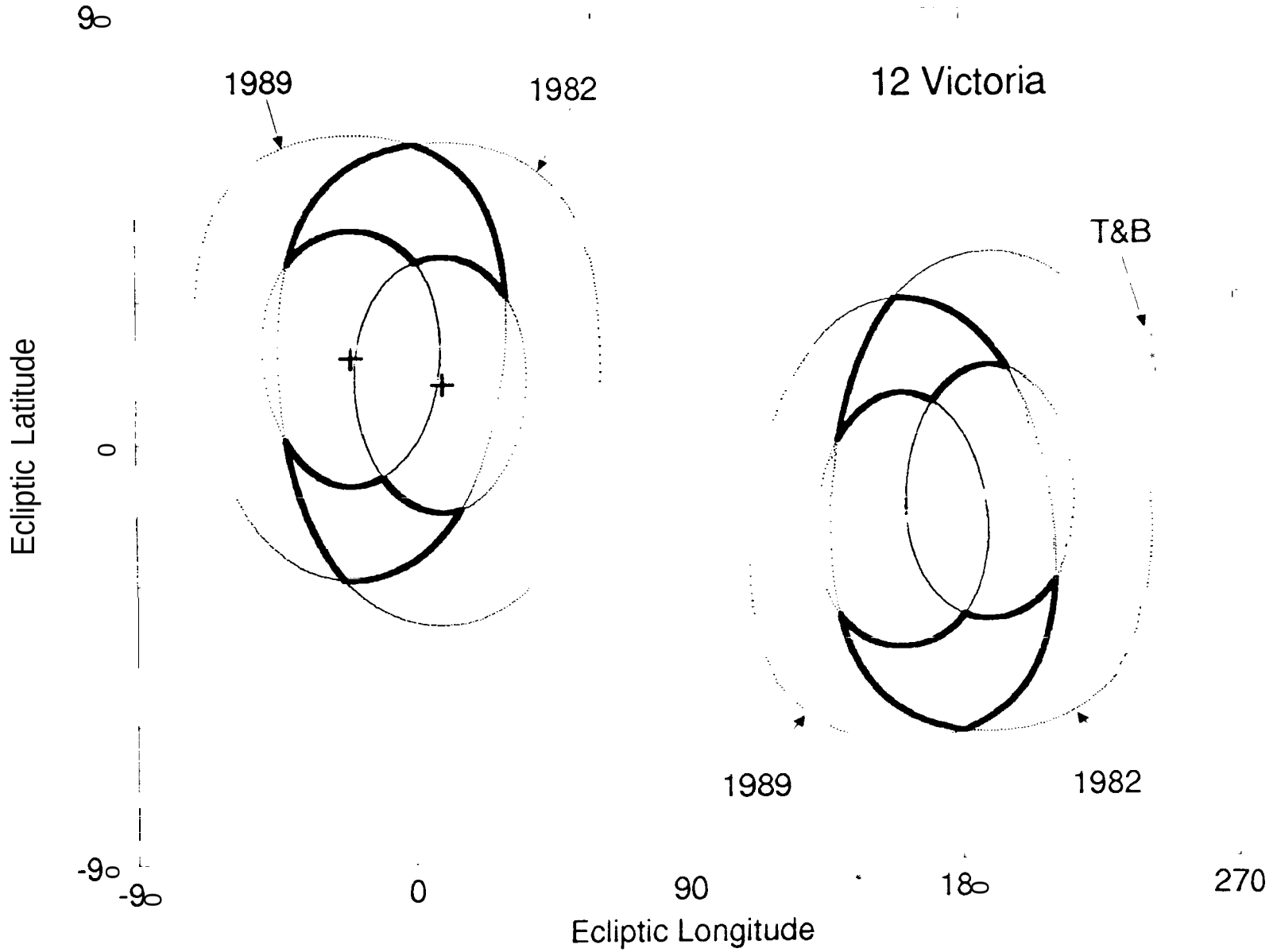
12 Victoria
1989
1982
T&B
1989
1982
9o
0
-9o
-9o
0
90
18o
270
Ecliptic Latitude
Ecliptic Longitude

Figure 19 (a)

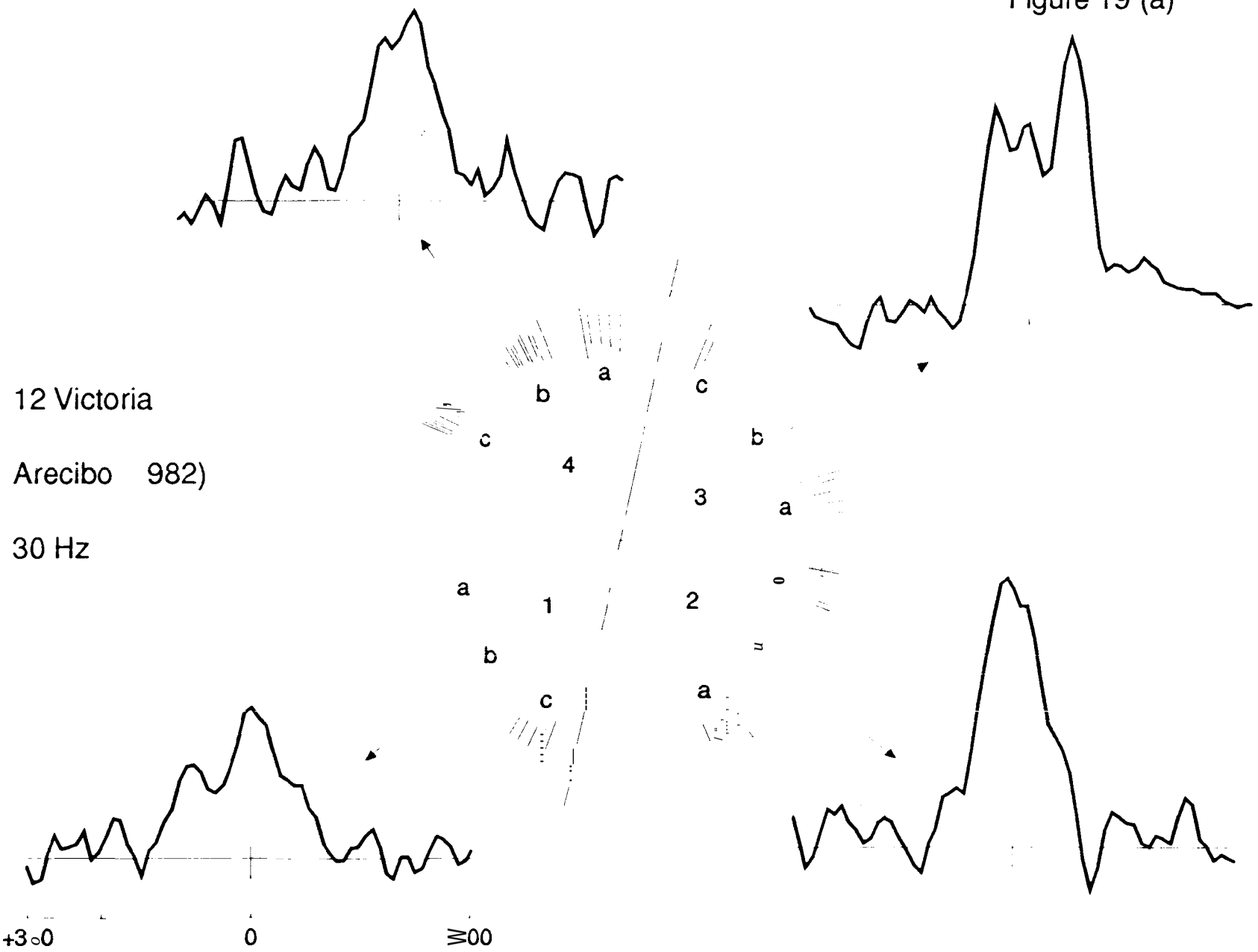

Figure 19 (b)

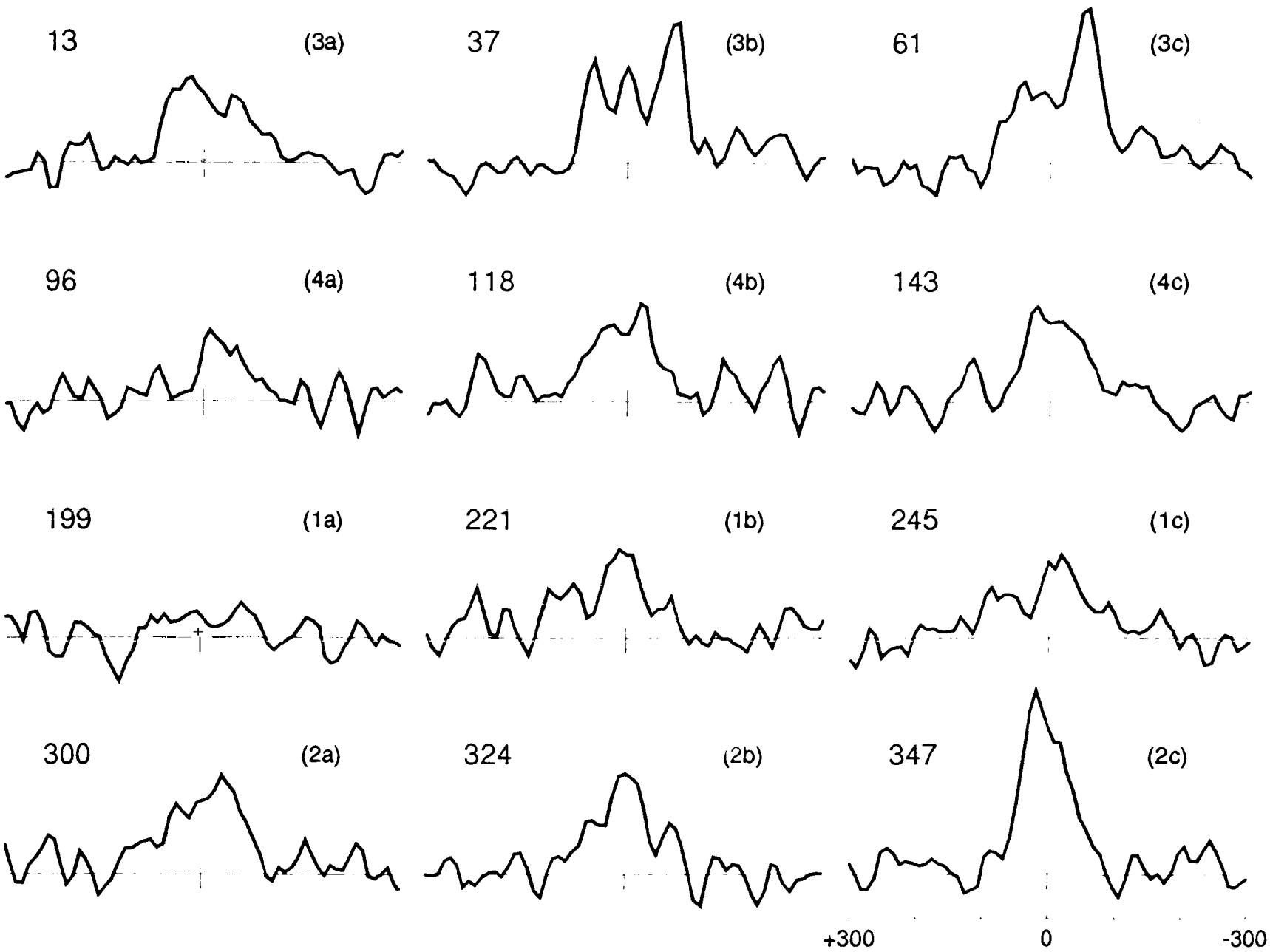
13
(3a)
37
(3b)
61
(3c)
96
(4a)
118
(4b)
143
(4c)
199
(1a)
221
(1b)
245
(1c)
300
(2a)
324
(2b)
347
(2c)
+300
0
-300

Figure 2o (a

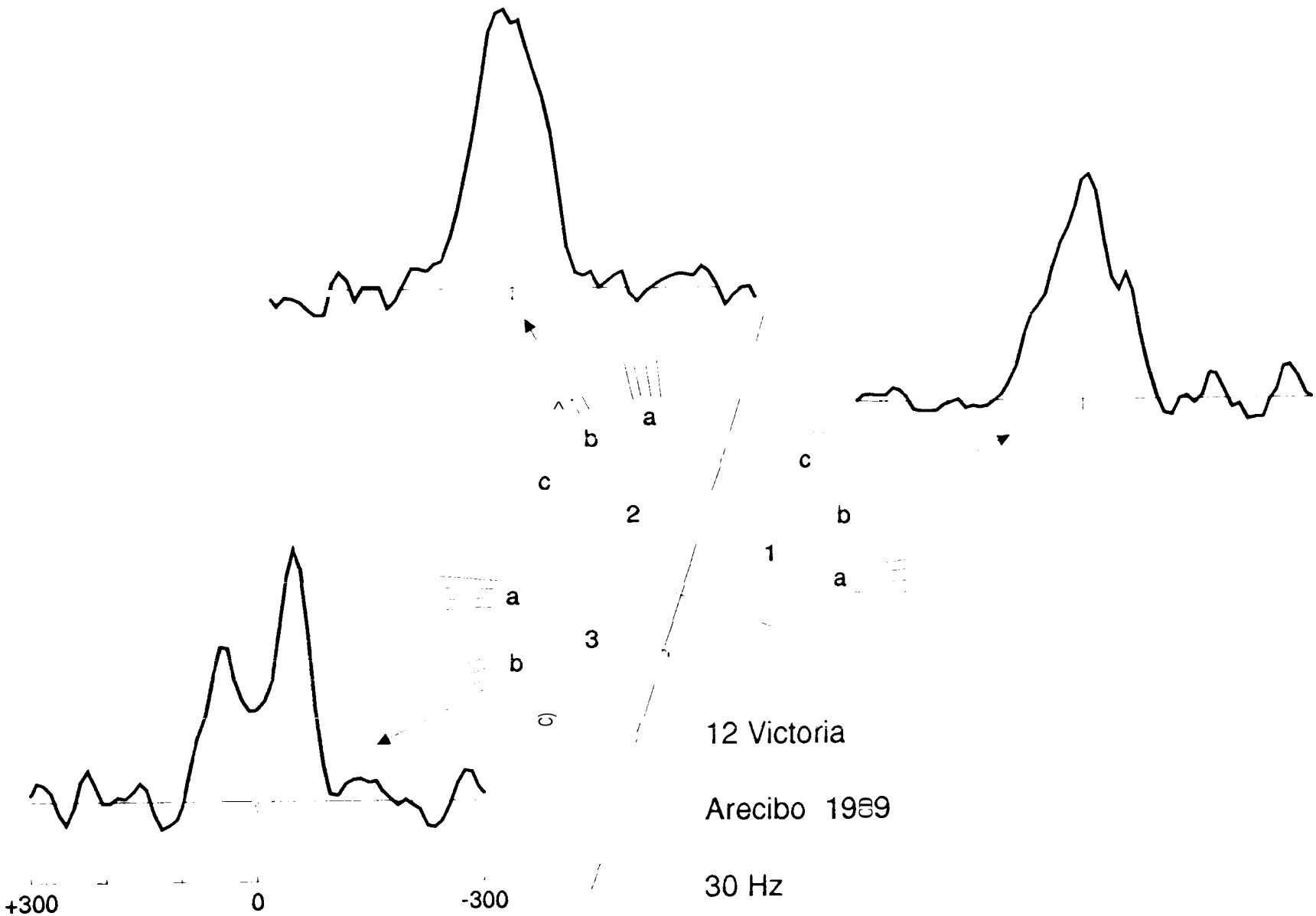

12 Victoria

Arecibo 1989

30 Hz

Figure 20 (b)

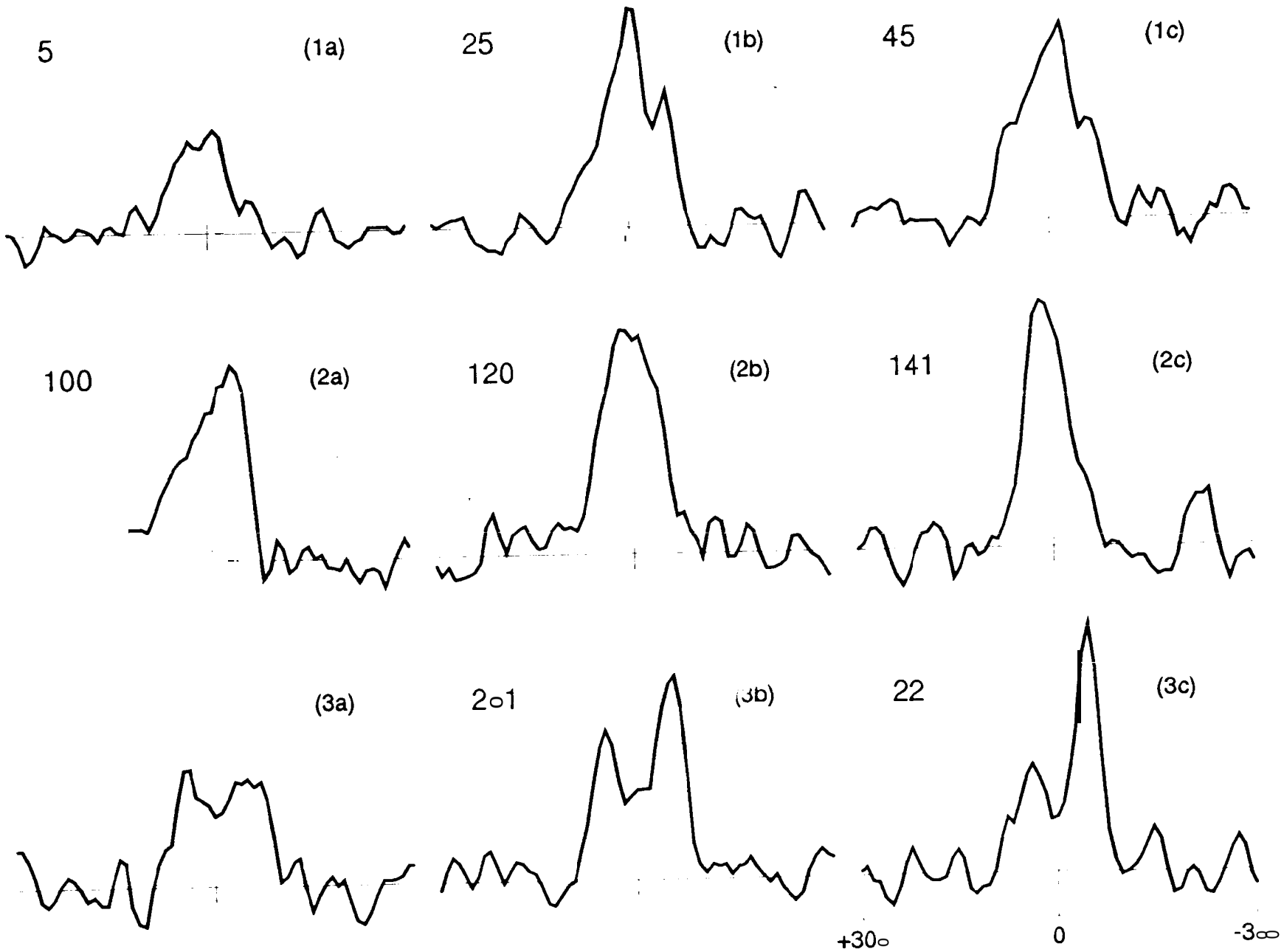

Figure 2 (a)

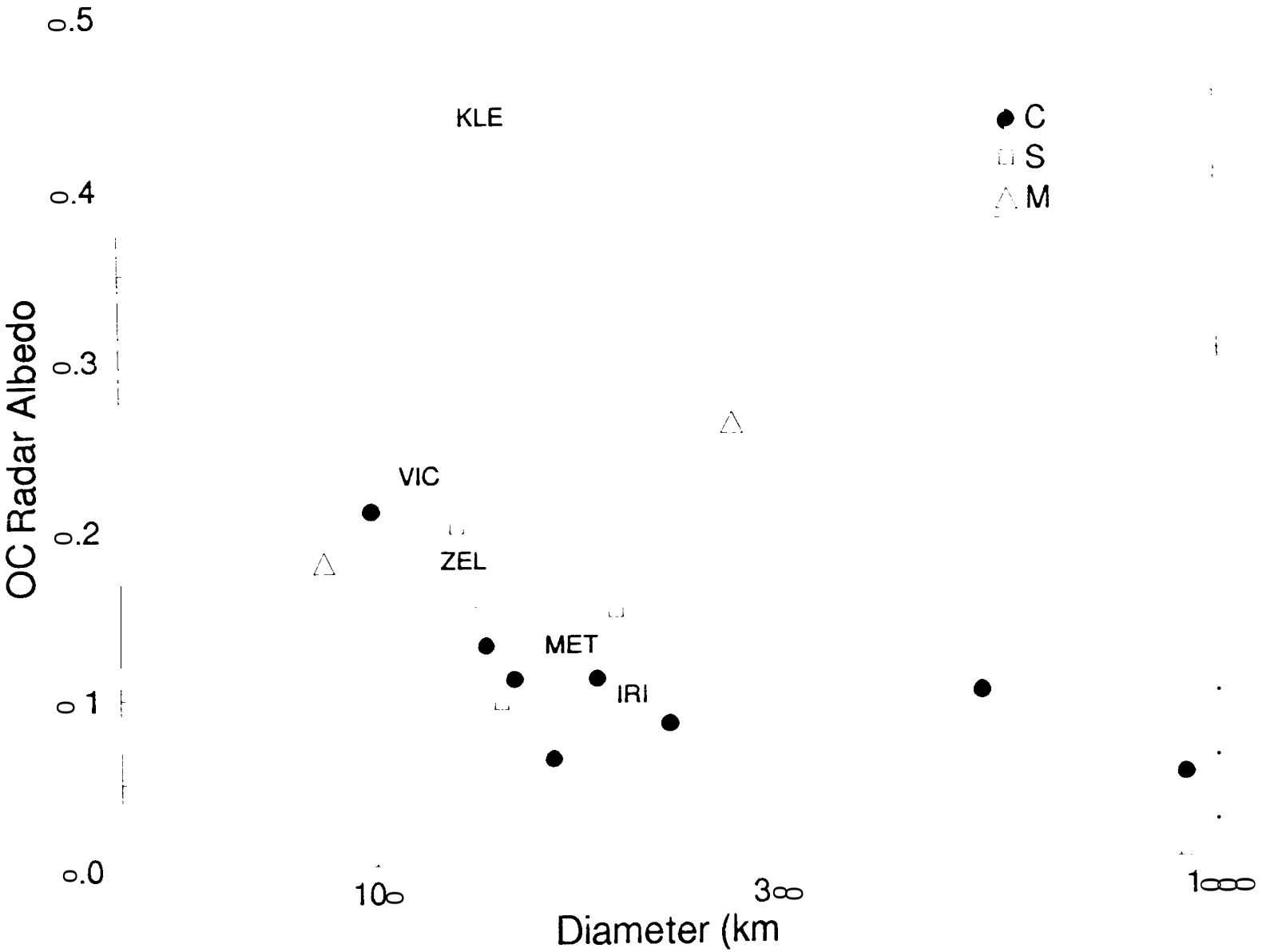
0.5
0.4
0.3
0.2
0.1
0.0
OC Radar Albedo
KLE
C
S
M
VIC
ZEL
MET
IRI
10∞
3∞
1∞∞
Diameter (km

Figure 21 (b)

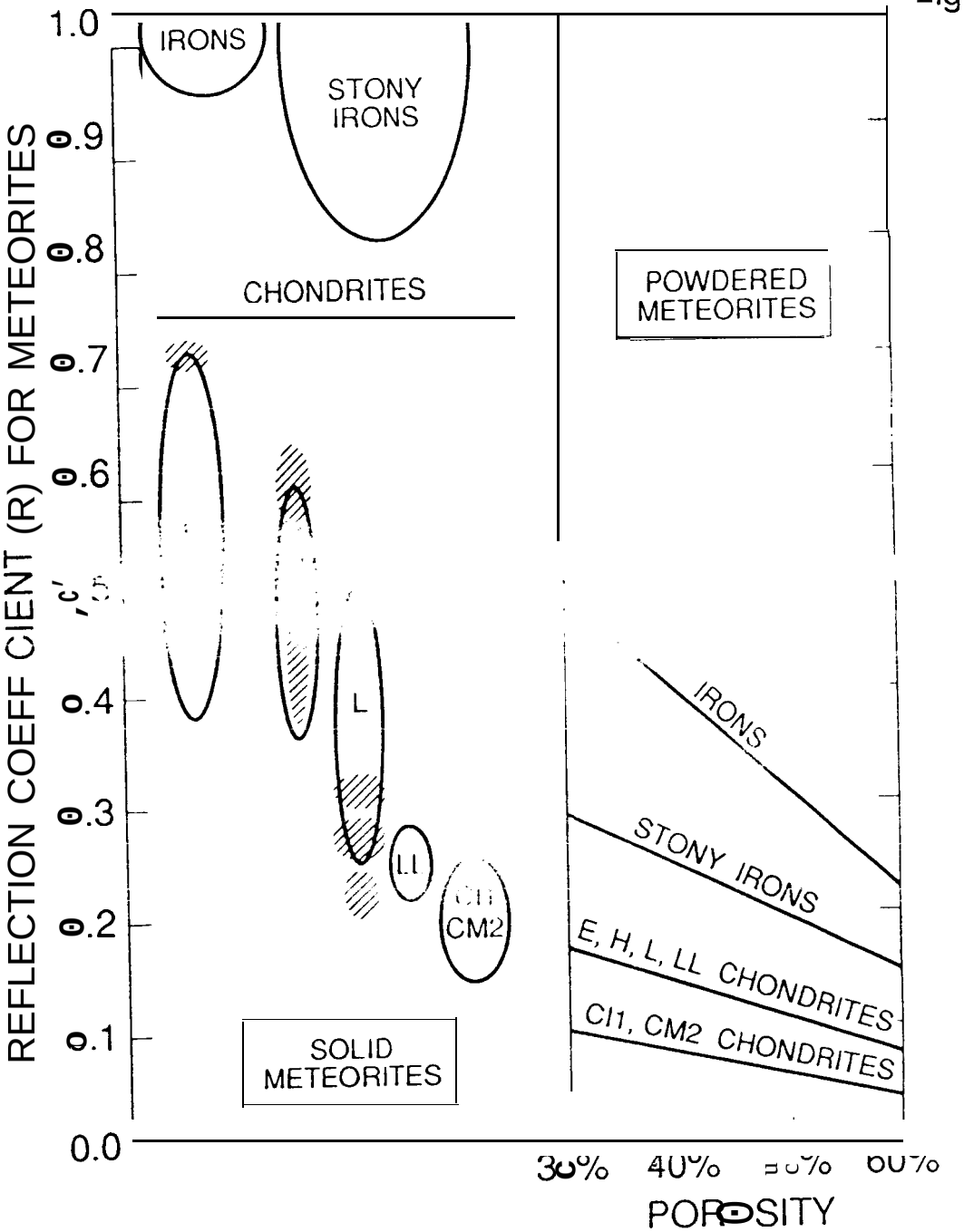
REFLECTION COEFF CIENT (R) FOR METEORITES
1.0
0.9
0.8
0.7
0.6
0.5
0.4
0.3
0.2
0.1
0.0
IRONS
STONY IRONS
CHONDRITES
POWDERED METEORITES
L
LL
CM2
SOLID METEORITES
IRONS
STONY IRONS
E, H, L, LL CHONDRITES
CI1, CM2 CHONDRITES
30%
40%
POROSITY